OPEN ACCESS

EUROPEAN MECHANICAL SCIENCE

E-ISSN: 2587-1110

2023 | VOL. 7 (1)

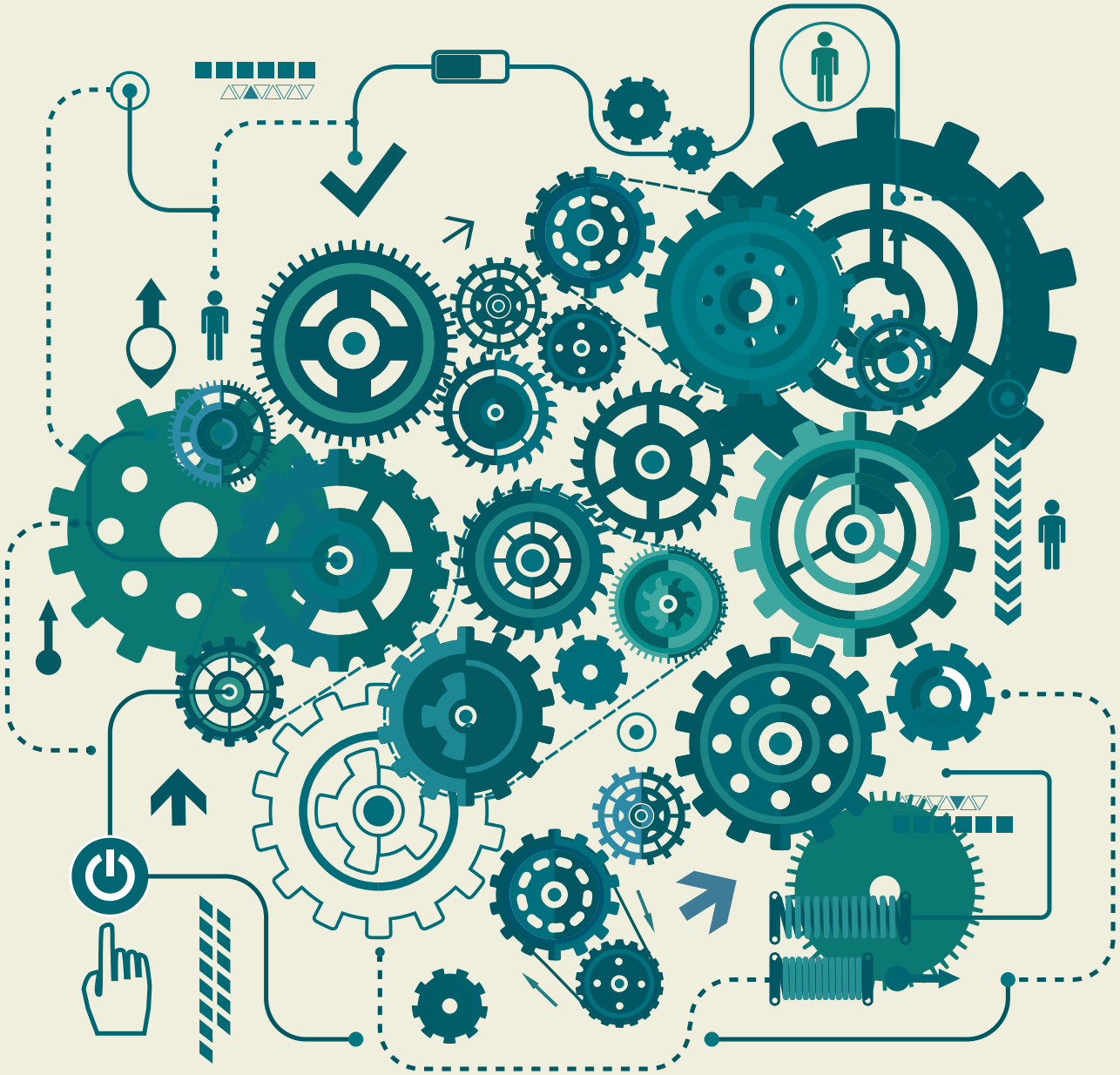

https://dergipark.org.tr/ems

TR DİZİN

Indexed / Abstracted in:

TR-Dizin, EXALY Full-Text Search Engine, Index Copernicus, Root Indexing, Google Scholar, Harvard University Library, Scilit, journaltocs, Sobiad Fatcat, Cite Factor

Aims and Scopes

European Mechanical Science (EMS) is an international, peer reviewed journal which publishes full length original research papers, reviews related to all areas of Mechanical Engineering such as: Solid Mechanics, Materials Engineering, Automotive Engineering, Fluid Mechanics, Thermal Engineering, Engine and Power Engineering, Dynamics & Control, Robotics & Mechatronics, Transportation Engineering, Computational Mechanics, Design, Systems, Manufacturing, Bio-Medical Engineering; Process Engineering, Aerospace Engineering. No charges are required from the Authors to publish the articles.EMS is a quarterly published journal operating an online submission and peer review system. It allows authors to submit articles online and track their progress via its web interface.

https://dergipark.org.tr/ems

Contents

– *Research Articles*

EUROPEAN MECHANICAL SCIENCE
e-ISSN: 2587-1110

Research Article

Effects of vacuum infusion configuration on homogeneity of glass fiber reinforced polymer composites for automotive components

Şafak Yıldızhan

Çukurova University, Engineering Faculty, Automotive Engineering Department, TR-01330, Adana, Turkey.

ORCID: Ş. Yıldızhan (0000-0002-8981-9869)

Abstract: In this study, the effects of vacuum infusion configuration on the homogeneities of glass fiber reinforced vinyl ester composites have been evaluated. Three different sizes of samples (100x100 mm, 500x500 mm, and 1000x1000 mm) were fabricated. Three different configurations were used to fabricate the samples. The first two configurations had one inlet, while the third configuration had two inlets for resin infusion. Thickness variations and hardness (Shore D) measurements were performed to determine the homogeneities of the samples. The results revealed that, for small size samples, the configurations have no obvious effect on the homogeneity of the samples, both in terms of thickness variations and hardness values. However, for larger samples, the configuration where the resin is introduced into the preform in the center of the component showed better homogeneity than other configurations. Even a better distribution is assessed with the introduction of the resin in the center of the sample, although this configuration also resulted in thickness swellings in the central areas of the sample. The thickness swellings were observed around the inlet areas for all configurations. The study shows that the resin flow in the center of the component is preferable but thickness swelling must be considered when dimensional tolerances are critical.

Keywords: Vacuum Infusion Configuration, Homogeneity, Glass Fiber Composite, Automotive

1. Introduction

Lightweighting is currently one of the main issues in the automotive industry due to environmental concerns [1]. Producing lighter, more cost effective and eco-friendly vehicles without compromising vehicle safety and product quality is a difficult task. At this point, composite materials are coming to the forefront in the automotive industry. Glass fiber reinforced plastics (GFRPs) composites have been one of the most preferred materials for automotive component manufacturing. GFRP composites have superior advantages such as very high specific strength (strength to density ratio), specific modulus (modulus to density ratio), and high corrosion resistance [2].

GFRP composites are produced with various techniques such as hand lay-up, spray-up, resin transfer molding (RTM), BMC (bulk molding compound) and SMC processes (sheet molding compound) filament winding, and resin infusion processes [3,4]. Vacuum assisted resin infusion molding (VARIM) (shortly named as vacuum infusion, also called VARTM, VM, SCRIMP etc.) process has the optimum properties among the techniques for low volume production of large scale products [5]. Processes such as RTM, BMC, SMC, and filament winding are the processes for mass production and those processes require high tool investments. VARIM processes, on the other hand, is suitable for low volume of production and its most critical advantage is the minimizing the air cavities that have negative effects on mechanical properties of the material in the composite structure. VARIM techniques are applied by stacking the layers on the mold until the desired thickness is reached and after that vacuum is applied to remove air inside the mold cavity. The matrix material (liquid resin) is introduced to the preform via vacuum force and the excess resin is removed from the layers [6]. With this technique, it is possible to fabricate composite materials with minimum resin usage and no air cavities in the material structure that deteriorates the mechanical properties. van Oosterom et al. (2019) compared six different vacuum infusion processes (VARTM, SCRIMP, CAPRI, DBVI, VAP, and PI) and they reported that there is no significant difference in void content of the samples in comparison with each other [7]. Abdurohman et al. (2018) compared the tensile properties of glass fiber reinforced composites with respect to their fabrication methods. The authors fabricated sam-

* Corresponding author.
Email: yildizhans@cu.edu.tr

European Mechanical Science (2023), 7(1): 1-6
https://doi.org/10.26701/ems.1166710
Received: August 25, 2022 — Accepted: December 22, 2022

ples with hand lay-up, vacuum bagging and vacuum infusion methods. They reported that samples produced with vacuum infusion method had the highest tensile strength and modulus elasticity among the samples [8]. Another important feature of the VARIM techniques that make it attractive is allowance to produce large-scale products [9]. Besides its advantages, VARIM processes also have some disadvantages. Thickness variation is one the major problems with the technique. Many researchers published studies focusing on better understanding and development of VARIM processes. Yenilmez et al. (2011) studied on minimizing the thickness variation by adjusting the injection conditions. The authors reported that the maximum thickness variation was significantly decreased by controlling pening/closing injection/ventilation gates and changing the pressure of the gates [10]. Ricciardi et al. (2013) proposed a different vacuum infusion method called pulsed infusion and they reported that the pulsed infusion improves flexural properties of the composite samples in comparison with conventional vacuum infusion [9].

In this study, the effects of vacuum infusion configuration and surface area on homogeneity of glass fiber reinforced vinyl ester composites have been investigated experimentally. Three different configurations were applied to three different sizes of samples. The thickness variations and hardness values were measured to evaluate the optimum configuration.

2. Material and Method

2.1. Materials

The experimental studies were conducted at laboratories of Automotive Engineering Department, Çukurova University. The glass fibers (biaxial, 300 gr/m^2, 0/90) and vinyl ester resin were purchased and used as received. The properties of the matrix material used for the study are given in Table 1.

2.2. Fabrication of the Samples

Glass fiber/vinyl ester composites were fabricated with vacuum assisted resin infusion process. For production, 3 different configurations were used for different scale samples. For the first configuration (a), the resin was supplied from one side of the preforms and vacuum vent was mounted on the cross side of the preform. For the second configuration (b), the vacuum vent was mounted in the middle of the preform. The resin was introduced from two points in the third configuration (c) and the vacuum vent was mounted on the other side of the preform. The experimental configurations are illustrated in Figure 1 schematically. Also, the photographs given in Figures 2-4 show the application of the configurations. For the experimental studies, total 9 samples (Table 2) were fabricated with configurations above and 3 different sample size. The sizes were selected as 100x100 mm , 500x500 mm and 1000x1000 mm. Each of the samples were fabricated with 5 layers of biaxial glass fibers and vinyl ester resin.

2.3. Testing of The Samples

After the complete curing of the samples (kept as vacuumed and sealed for 24 hours), they were removed from the glass table and each sample was cut into smaller pieces. The thickness values of the samples were measured (at least 5 measurements were recorded for each piece with micrometres and average values calculated) and hardness tests were conducted. The hardness values of the samples were measured with HT-6510D Shore D hardness tester (for each piece at least 5 measurements were conducted). The measurements were not taken from points which are closer to the edges less than 10 mm.

3. Results and Discussions

The experimental samples were fabricated with vacuum infusion technique. The infusion progresses of the configurations are shown in Figures 5-7. The thickness of the samples was measured to determine the dimensional homogeneity through the fabrication process. In infusion-like processes it is quite difficult to produce components with high dimensional tolerances. In Figures 8-10, the thickness measurement results are shown in colormaps.

The thickness measurements showed that, the material thickness varies especially at regions of resin inlet and outlet. The thickness variations were observed for all samples as it is seen in Figures 8-10. For the low surface area samples (100x100 mm), the configuration (c) which had two resin inlet showed slightly better dimensional homogeneity even it had highest thickness variation among the samples. The maximum thickness variation (MTV) values were 0.18, 0.14, and 0.2 mm for configurations a, b, and c, respectively. With the increment of surface area, the MTV values increased which leads to lower dimensional homogeneity. The MTV values of 500x500 mm samples were measured as 0.2, 0.14, and 0.25 mm for configurations (a), (b), and (c), respectively. Those values were 0.3, 0.14 and 0.3 mm for 1000x1000 mm samples. In Figures 11-13, hardness values (Shore D) of the samples are illustrated as colormaps. The hardness measurements revealed that regions thicker regions had lower hardness values due to accumulation of the resin. The thicker regions can also be seen as resin rich which leads

Table 1. Properties of the matrix material

Material	Brand	Chemical	Ratio
Resin	Polives 702	Vinyl ester	-
Curing Agent	AKPEROX A60	Methyl Ethyl Ketone Peroxide	2% of resin (by weight)
Accelerator	AKCOBALT KXC6	Cobalt(II) 2-Ethyl Hexanoate	0.2% of resin (by weight)

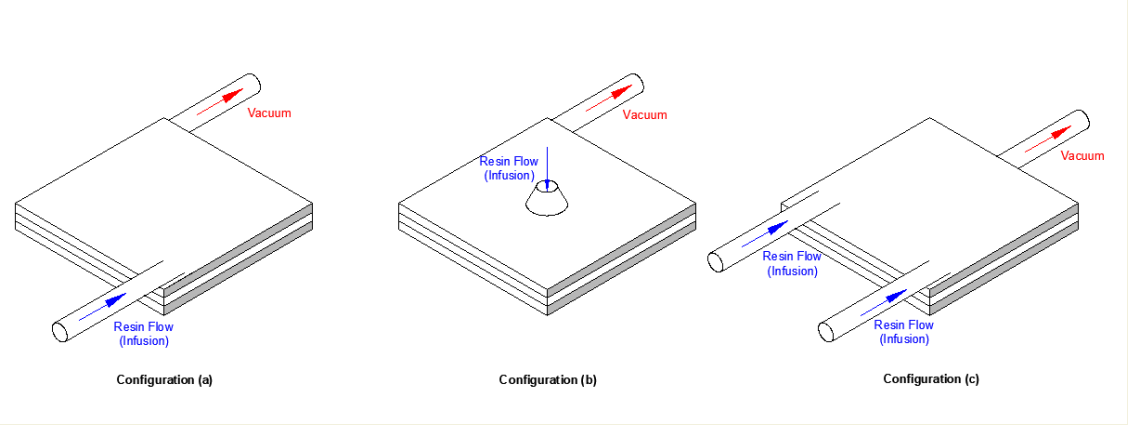

Figure 1. Schematics of the experimental configurations

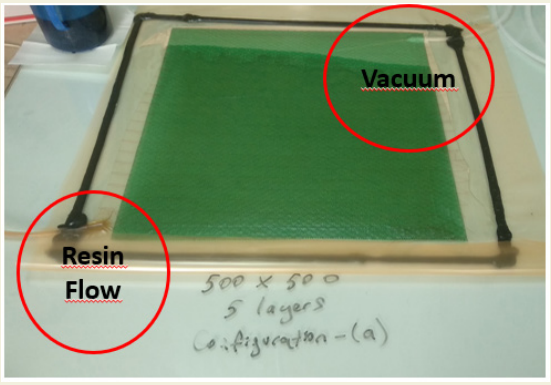

Figure 2. Photograph of the first experimental configuration (a)

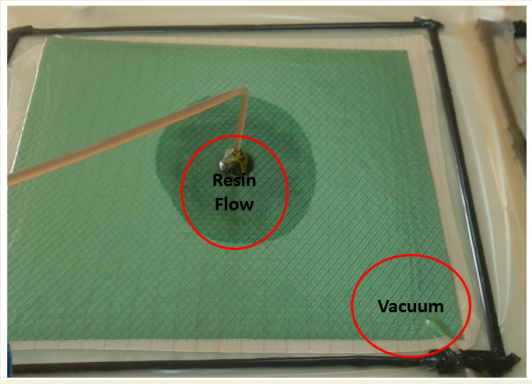

Figure 3. Photograph of the second experimental configuration (b)

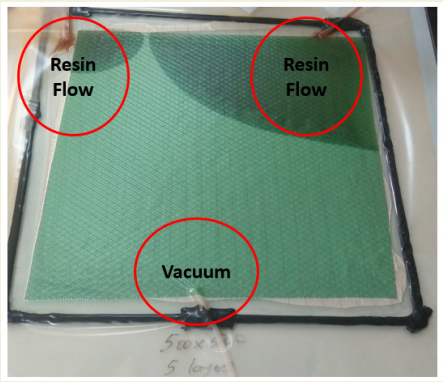

Figure 4. Photograph of the third experimental configuration (c)

Table 2. Experimental design

Specimen No	Specimen Size (length x width) (*mm*)	Surface Area (m^2)	Configuration
1	100x100	0.01	a
2	500x500	0.25	
3	1000x1000	1	
4	100x100	0.01	b
5	500x500	0.25	
6	1000x1000	1	
7	100x100	0.01	c
8	500x500	0.25	
9	1000x1000	1	

to lower fiber fraction ratios. For 100x100 mm samples, the hardness values increased with distance from the resin inlet areas for all configurations. The homogeneities of the samples were deteriorated with increment of the surface area for all configurations. But, configuration (b) showed a better distribution of hardness values than configurations (a) and (c) when surface area increased. For the small surface area, there is no evident difference among the configurations. The thickness and hardness measurements revealed that, configuration (b) which the resin inlet is placed in the middle of the samples shows better homogeneity than other configurations when the surface area is large. But, in contrary, that configuration causes to thickness swelling and low hardness in the middle area of the sample which may create critical problems for the composite products.

4. Conclusions

In this study, the effects of vacuum infusion configuration on different scales glass fiber reinforced polymer composites were investigated to determine the optimum configuration for automotive composite components and the followings were concluded;

- VARIM is an effective technique to produce composite components. With VARIM processes, the air

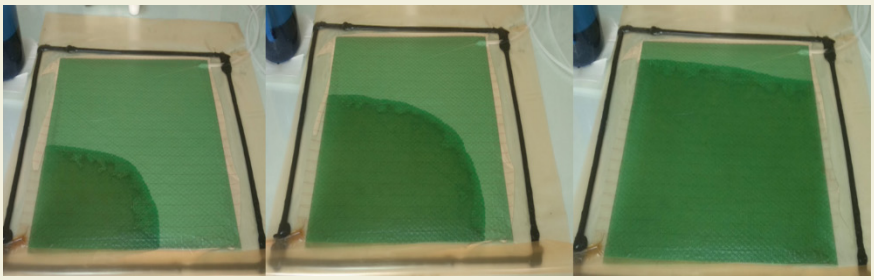

Figure 5. Infusion progress of configuration (a)

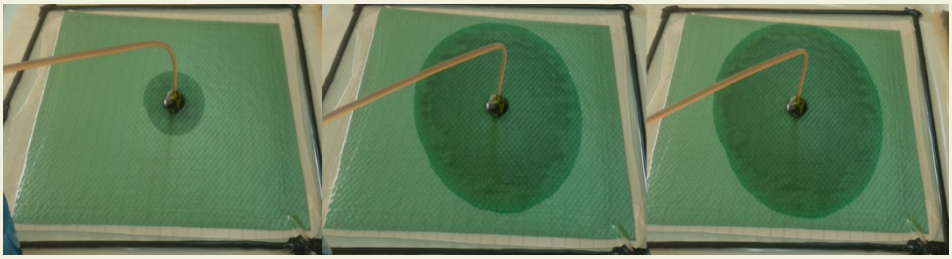

Figure 6. Infusion progress of configuration (b)

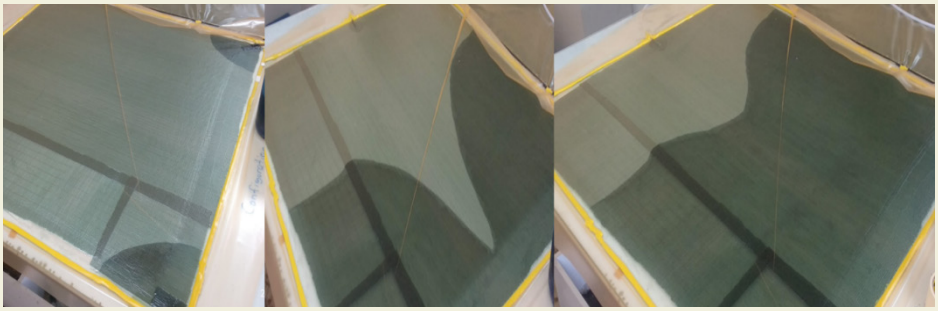

Figure 7. Infusion progress of configuration (c)

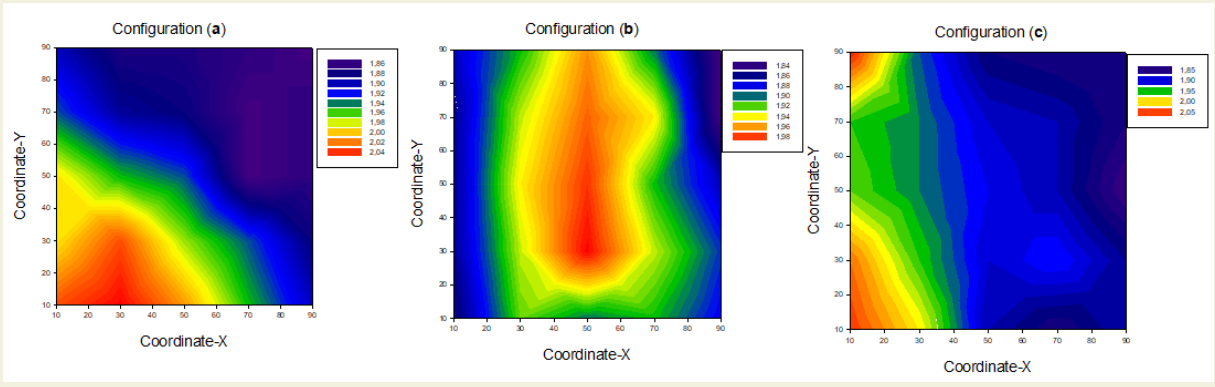

Figure 8. Thickness values of the 100x100 mm samples

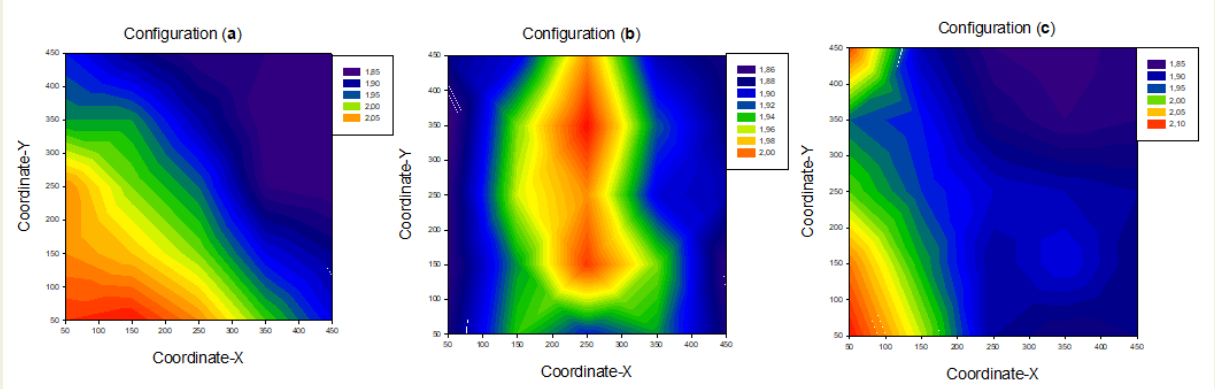

Figure 9. Thickness values of the 500x500 mm samples

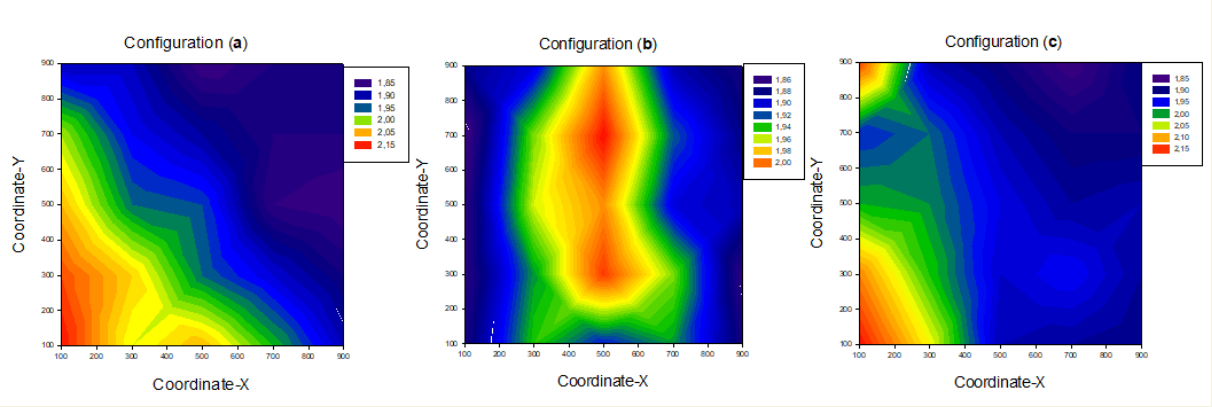

Figure 10. Thickness values of the 1000x1000 mm samples

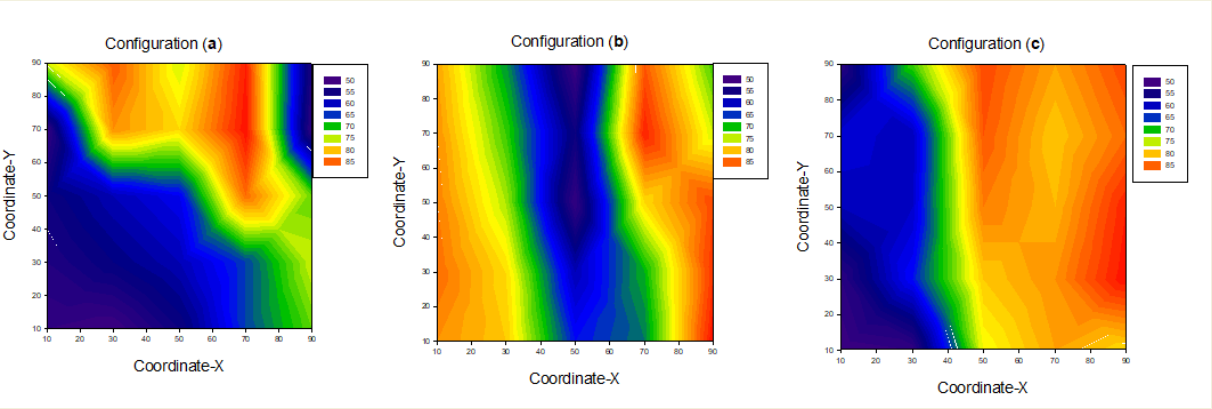

Figure 11. Hardness values of the 100x100 mm samples

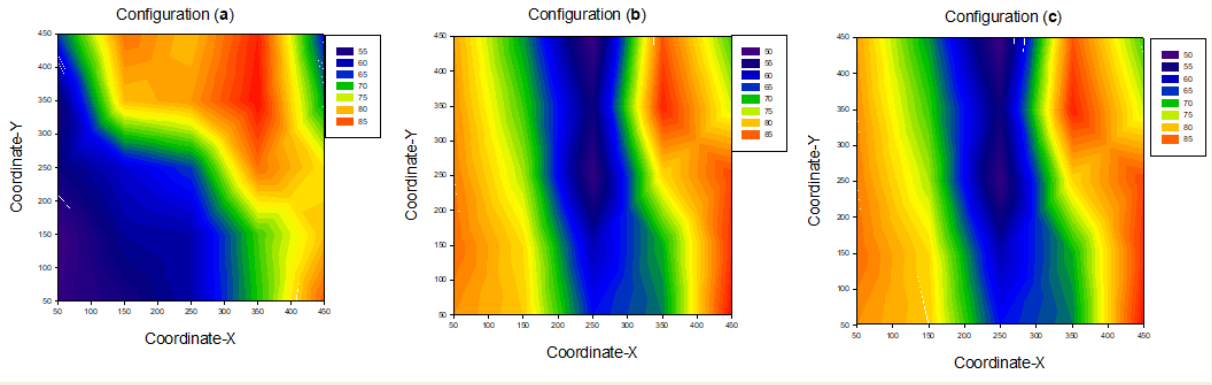

Figure 12. Hardness values of the 500x500 mm samples

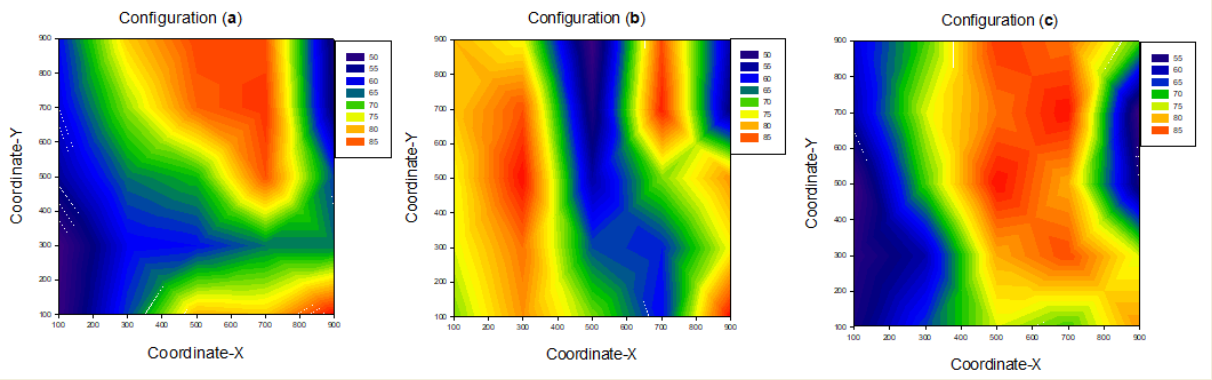

Figure 13. Hardness values of the 1000x1000 mm samples

cavities inside the components are removed and thus better mechanical properties are obtained.

- In VARIM processes, thickness swellings occur in the regions of resin inlet. And thus, it is difficult to produce composite components with high dimensional tolerances.
- The homogeneity of the composite material deteriorates with the increment of surface area.
- For small surface area components, the configurations do not have evident effect on homogeneity.
- For large surface areas, configuration should be carefully selected. The configuration which resin is introduced in the middle of sample provides better distribution of the matrix material but, the thickness swelling in the middle of the component have to be considered.

5. References

[1] Akhshik, M., Panthapulakkal, S., Tjong, J., Sain, M., (2019). The effect of lightweighting on greenhouse gas emissions and life cycle energy for automotive composite parts. Clean Technologies and Environmental Policy. 21(3): 625–36. doi: 10.1007/s10098-018-01662-0.

[2] Sathishkumar, T.P., Satheeshkumar, S., Naveen, J., (2014). Glass fiber-reinforced polymer composites – a review: Http://Dx.Doi.Org/10.1177/0731684414530790. 33(13): 1258–75. doi: 10.1177/0731684414530790.

[3] Yıldızhan, Ş., Akar, M.A., Özcanlı, M., Serin, H., (2019). Manufacturing Methods of Polymer Matrix Composites: A Brief Review of Techniques Convenient for Mass Production. 4th International Mediterranean Science and Engineering Congress (IMSEC 2019), p. 395–9.

[4] Serin, H., Derici, O.B., Yıldızhan, Ş., (2019). A Review on Open Mold Techniques for Polymer Matrix Composite Products | AVESİS. 4th International Mediterranean Science and Engineering Congress (IMSEC 2019), p. 400–4.

[5] Correia, N.C., Robitaille, F., Long, A.C., Rudd, C.D., Šimáček, P., Advani, S.G., (2005). Analysis of the vacuum infusion moulding process: I. Analytical formulation. Composites Part A: Applied Science and Manufacturing. 36(12): 1645–56. doi: 10.1016/j.compositesa.2005.03.019.

[6] Ouezgan, A., Mallil, E.H., Echaabi, J., (2022). Manufacturing routes of vacuum assisted resin infusion: Numerical investigation. Journal of Composite Materials.: 002199832211114. doi: 10.1177/00219983221111492.

[7] van Oosterom, S., Allen, T., Battley, M., Bickerton, S., (2019). An objective comparison of common vacuum assisted resin infusion processes. Composites Part A: Applied Science and Manufacturing. 125: 105528. doi: 10.1016/j.compositesa.2019.105528.

[8] Abdurohman, K., Satrio, T., Muzayadah, N.L., Teten., (2018). A comparison process between hand lay-up, vacuum infusion and vacuum bagging method toward e-glass EW 185/lycal composites. Journal of Physics: Conference Series. 1130(1): 012018. doi: 10.1088/1742-6596/1130/1/012018.

[9] Ricciardi, M.R., Antonucci, V., Durante, M., Giordano, M., Nele, L., Starace, G., et al., (2014). A new cost-saving vacuum infusion process for fiber-reinforced composites: Pulsed infusion. Journal of Composite Materials. 48(11): 1365–73. doi: 10.1177/0021998313485998.

[10] Yenilmez, B., Akyol, T., Caglar, B., Sozer, E.M., (2011). Minimizing Thickness Variation in the Vacuum Infusion (VI) Process. Advanced Composites Letters. 20(6): 096369351102000. doi: 10.1177/096369351102000603.

EUROPEAN MECHANICAL SCIENCE
e-ISSN: 2587-1110

Research Article

Numerical investigation of different combustion chamber on flow, combustion characteristics and exhaust emissions

İlker Temizer[1], Ömer Cihan[2], Öncel Öncüoğlu[3]

[1]Sivas Cumhuriyet University Technology Faculty, Department of Manufacturing Engineering, 58140, Sivas, Turkey.
[2]Hakkari University, Engineering Faculty, Department of Mechanical Engineering, 30000, Hakkari, Turkey.
[3]Istanbul Technical University, Faculty of Mechanical Engineering, Department of Mechanical Engineering, 34469, Istanbul, Turkey.

ORCID: İ. Temizer (0000-0003-1170-3898), Ö. Cihan (0000-0001-8103-3063), Ö. Öncüoğlu (0000-0002-8377-5375)

Abstract: This study includes numerical analysis of diesel engines with different bowl geometry. Numerical analyzes of the diesel engine with asymmetrical bowl geometry were performed in Ansys Forte software. In the study, four-stroke, air cooled, a single-cylinder and direct injection diesel engine were used. It has been tested where the maximum torque is obtained as the operating condition at 2000 rpm. According to the results obtained from the analyzes, the new combustion chamber system geometry provided a 40.3% reduction in soot emissions while NO emissions increased slightly with the 8-cavity bowl geometry created in the chamber compared to the standard combustion chamber system. Increasing air velocity, and turbulent kinetic energy values in the chamber affected the evaporation levels of the fuels. As a result, the improved mixture formation caused a decrease in incomplete combustion products (CO, HC and soot). The new combustion chamber system geometry according to standard combustion chamber system type, an increase of approximately 4.2% occurred in the calculated squish rates. It has been observed that the increase in the bowl surface area causes the combustion, and thus the temperature to spread over a larger area on the piston.

Keywords: Diesel engine; Bowl geometry; Combustion analysis; Fuel spray distribution.

1. INTRODUCTION

In recent years, engine manufacturers have increased their research to reduce emissions due to awareness of air pollution and strict emission rules. In addition, many studies are carried out on the parameters affecting engine performance and combustion. In internal combustion engines, diesel engine produces better fuel consumption, higher exhaust emission value and higher noise than gasoline engine. Low fuel consumption in diesel engines is used in many areas such as electric power generation, transportation and agricultural machinery [1]. There are many parameters such as fuel specifications, operating conditions and engine constructive design, which are the main factors such as efficiency, combustion characteristics and emissions of a compression ignition engine [2].

A fast and better air-fuel mixture is the most important need for reducing exhaust emissions, improving engine performance and combustion characteristics. For the mixing quality of diesel fuel injected into the combustion chamber with air, the geometry of the combustion chamber, the injection parameters, and the characteristics of the air movements should be improved [3]. Combustion chamber geometry has an important place in the design of diesel engines. For a good geometry, the air-fuel mixture should be improved, and for easier evaporation, there should be more air movement in the cylinder in terms of swirl, squish and turbulence [4]. Singh et al. [5] stated that with different combustion chamber geometries, the desired tumble, swirl, squish and turbulence parameters in the combustion chamber can be improved, thereby lowering exhaust emissions and improving engine performance.

Saito et al. [6] compared the bowl geometries conventional and re-entrant in a single-cylinder, four-stroke, direct injection diesel engine. Engine performance, NOx and soot emissions, and combustion parameters were investigated. As a result, the ignition delay is reduced due to the fact that the re-entrant geometry is hotter than the other, the wall where the fuel hits. Moreover, turbulence increased with the increase of in-cylinder air movements, and combustion improved. Yaliwal et al. [7] reported that the Re-entrant type combustion chamber showed maximum performance under 230 bar injection pressure, four holes and 0.25 mm nozzle opening con-

* Corresponding author.
Email: omercihan@hakkari.edu.tr

European Mechanical Science (2023), 7(1): 7-15
https://doi.org/10.26701/ems.1181494
Received: September 28, 2022 — Accepted: December 8, 2022

ditions. Bapu et al. compared Modified Hemispherical Combustion Chamber (MHCC) and conventional Hemispherical Combustion Chamber (HCC) designs by using ANSYS fluent software in a diesel engine. According to the results obtained, it was seen that the mixture formation was better when the flow movements at different positions of the piston were examined compared to the HCC [8]. Optimum bowl geometry improves air/fuel mixture formation, and reduces rich mixing zones [9]. Both NO_x emissions, and local high temperatures can be controlled by avoiding in-cylinder rich mixing zones [10]. Otherwise, Şener et al. [11] observed which the geometry of the piston bowl has a significant effect on the in-cylinder pressure, in-cylinder temperature, heat release, and exhaust emission values in used engine. In the numerical study using CONVERGE software, DA, DB, DC, DD, DE and DF geometries were used. DF and DE geometries have higher heat release rate, in-cylinder pressure and temperature values due to the main radius of bowl. However, NOx emissions have also increased.

Li et al. [12] numerically and experimentally compared the geometry of the double swirl combustion system (DSCS) and lateral swirl combustion system (LSCS) in a compression ignition engine at different speeds. The influence of LSCS geometry on fuel economy, and soot emissions was investigated. LSCS provided 2.8–4.1g / kWh fuel economy compared to DSCS, and soot exhaust emissions decreased in the range of 69–75%. The bowl shape of the piston directly affects the factors of swirl, squish, tumble, turbulence and flame velocity. Therefore, it causes changes in combustion characteristics and exhaust emissions [13-15].

Air movements in internal combustion engines have a significant effect on fuel/air mixture formation. In this study, a total of eight (8) bowls created on the piston will increase the airflow both in the horizontal and vertical axis. Also, the multi-cavity spreading of the cavity on the piston head will cause the combustion hot surface area to increase. Directing the fuel assembly by striking it against the combustion chamber surface also enables it to evaporate more easily, resulting in reduced ignition delay times. By injecting the fuel to the point where the two cavities meet, the fuel beam will be directed to different cavities and the combustion will be mixed with more air in more than one region. In addition, it is aimed to reduce the thermal stresses on the piston by preventing regional temperature formations by realizing a greater distribution of combustion on the piston surface with this geometry. Starting the evaporation process before the fuel reaches the center of the cavity prevents the fuel from breaking down at high temperatures and reduces the formation of C (soot) emissions to minimum levels. With this geometry, the fuel assembly sprayed by the injector with four nozzles will hit the wall at the junction of the two cavities and will both evaporate with the effect of temperature and be directed towards the cavity center where there is high air movement. In this case, instead of multi-hole injectors and high injection pressures, full combustion can be achieved by using a hole injector with different cavities and low injection pressures which makes it possible to significantly reduce the incomplete combustion products C (PM- particulate matter), CO and HC values.

In this study, a new combustion chamber system (NCCS) with different geometry was analyzed using Ansys Forte software. The obtained results were compared with the standard combustion chamber system (SCCS). The diameter of the piston's bowl bottom base was numerically investigated for R3 =3 mm (NCCS), R3=4 mm (NCCS_V1) and R3 =5 mm (NCCS_V2) in geometry, and some results have been obtained. The effects of this diameter in the bowl geometry on in-cylinder pressure and temperature, instantaneous and cumulative heat release rate, swirl ratio, turbulent kinetic energy and exhaust emissions (CO, CO2, soot, UHC and NO) were investigated. Moreover, the flow properties (temperature, velocity and TKE changes) of the bowl geometries were researched.

2. NUMERICAL STUDY

In order to determine the boundary conditions in a model, it must be tested under different operating conditions. Here, mentioned model was created according to the main dimensions and technical features of the four-stroke, direct injection ANTOR 3 LD 510 diesel engine. The technical data of the engine is given in Table 1. Ansys Forte software was used for the model. In-cylinder heat, flow, mixing, and combustion characteristics were investigated with this software. While NCCS and SCCS geometries were created in the program, the compression ratio of 17.5 (compression ratio of the engine) was kept constant. Generally, air flow movement from the TDC to the BDC decreases in engines. This has a great effect on the formation of the mixture. The NCCS bowl geometry consists of eight pockets. Boundary conditions in Table 2 were used. A detailed reduced chemical combustion mechanism, which has been accepted in many studies in the literature, has been used for make the exhaust emissions closer to reality. RNG k-epsilon turbulence model was used as it is more suitable for combustion analysis. A macro-dimensional examination was made, and it gave results in a short time compared to other models in terms of solution time with this model. This model is the most preferred type in the literature [16, 17]. Adaptive Collision Mesh model was used for droplet collision. One of the biggest advantages of this model is that it eliminates the dependency on the network structure. KH-RT hybrid model was applied for the breakup of the droplets, and the KIVA-based wall collision model was used for the droplets hitting the wall.

The gas force distribution in pockets has become more balanced with NCCS. No changes have been made to the structure and location of the injector, and the original injector data has been added to the software. Injector cone projection was applied according to SCCS type. One of the main criteria in the new design was the eight pocket

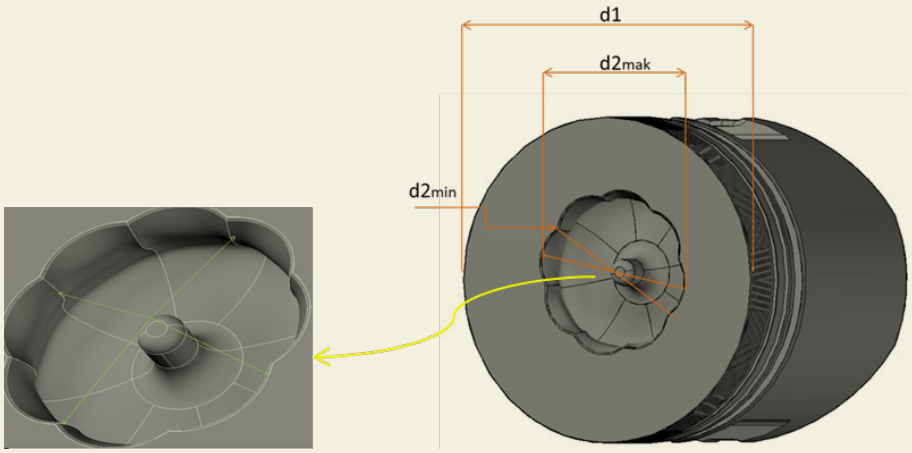

Figure 1. Piston bowl and fuel injection direction

Table 1. Technical properties of the test engine

Engine Name	Antor 3 LD 510
Engine Type	Four stroke, air-cooled, single-cylinder and direct injection diesel engine
Piston displacement	510 cm^3
Stroke x Bore	90 x 85 (mm x mm)
Compression ratio	17.5:1
Power	6.6@3000 (kW)
Torque	32.8@2000 (Nm)
Injection angle	126°
Injector hole number	4

Table 2. Simulation boundary conditions

Number of cylinders	Single cylinder
Type of cooling	Air-cooled
Bore	85 mm
Compression ratio	17.5
Crank radius	42 mm
Number of injection nozzle	4
Injection Timing (start and stop)	705° and 729° CA
Injection spray angle	160°
Injection rate (mass)	5.11e-6 kg
Engine speed	2000 rpm
Air inlet temperature	293.15 (K)
Air inlet pressure	1 (bar)
Fuel injection temperature	330.15 (K)
Turbulence model	RNG k-epsilon
Wall interaction model	Walljet1
Evaporation model	Multi component
Soot emission model	Kinetic model
NO emission model	Zeldovich model
Cylinder head temperature	575.15 (K)
Cylinder wall temperature	475.15 (K)

radii placed from the top of the piston. It is aimed to plaster the fuel on the wall, and to evaporate faster by making use of the wall temperature, and higher swirl with the NCCS geometry. It was observed that the mixture formation in the NCCS geometry was affected by the swirl rate at the end of the intake stroke.

Piston design in reciprocating engines is one of primary importance subject areas among engine parts. Many parameters such as compatibility with engine cylinders, combustion effect, and flow direction feature can be studied. In the present paper, it is aimed to find out the effect of changes to be made on the NCCS main geometry. In the new piston geometry designed in this direction, the geometric parameters of SCCS such as piston outer diameter, skirt part, and bowl depth were kept constant. In Fig. 1, some geometric lengths of NCCS are given. The bowl diameter, which is called d2 in SCCS geometry, has two different values in NCCS as maximum and minimum. Gradual narrowing of the bowl diameter of the NCCS is observed. It is known that small throat diameter, and swirl ratios affect NO emissions and heat transfer rate [18]. In order to create stronger flow mobility, a design that will increase the gradual flow rate in the throat design is presented. The zones where the fuel particles hit the wall, and their distribution are visually given in numerical analysis. The injection axis of the fuel particles in the bowl, and the zones of impact on the wall are shown in Fig. 1. It causes less energy loss with fuel sprayed on a wall with a round lip compared to a flat geometry [19]. The diameter of the piston's bowl bottom base was investigated, and the effect of the change in this diameter was examined.

3. RESULTS and DISCUSSION

Three different bowl bottom radius values were determined for NCCS in the Ansys Forte program, and the most ideal geometry was selected from the results, and compared with the SCCS values. Especially in hollow geometries, the bowl bottom radius has a great importance in

both air and fuel distribution. For this reason, the effect of different radius values on the geometry consisting of eight pockets was investigated. The diameter of the piston's bowl bottom base was numerically investigated for R_3 =3 mm (NCCS), R_3=4 mm (NCCS_V1) and R_3 =5 mm (NCCS_V2) in geometry, and some results have been obtained. It has caused a decrease in the swirl rate around TDC for all combustion chamber models, especially due to its cavity structure. It can be said that the swirl ratio of the standard geometry is achieved, and combustion and emissions are reduced significantly with the reduction of this radius (for R3 =3 mm). Numerical combustion analysis results of NCCS and SCCS are given in Fig. 2, Fig. 3, Fig. 4 and Fig. 5.

In all analyzes with NCCS geometry, it can be said that

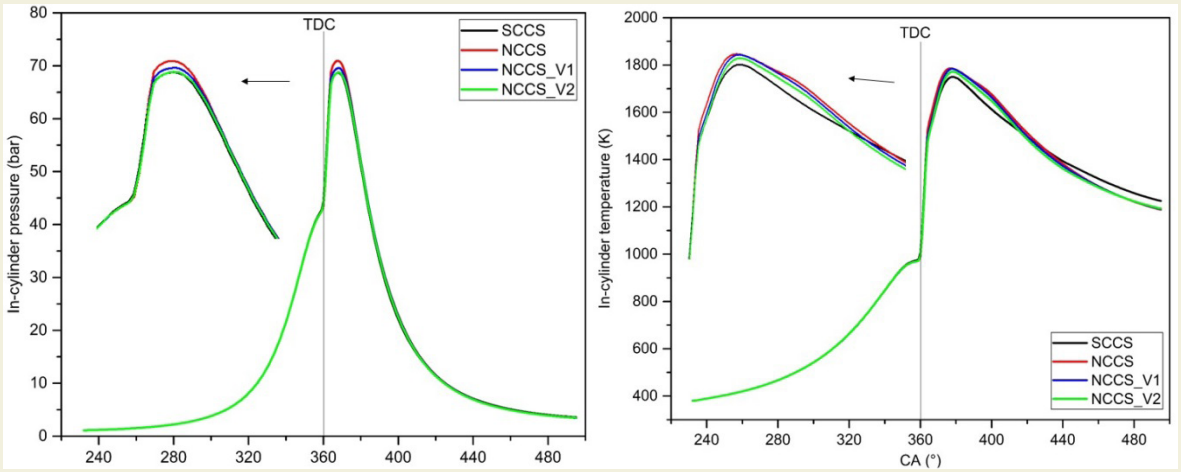

Figure 2. Change of in-cylinder pressure and temperatures with crank angle for NCCS and SCCS geometries

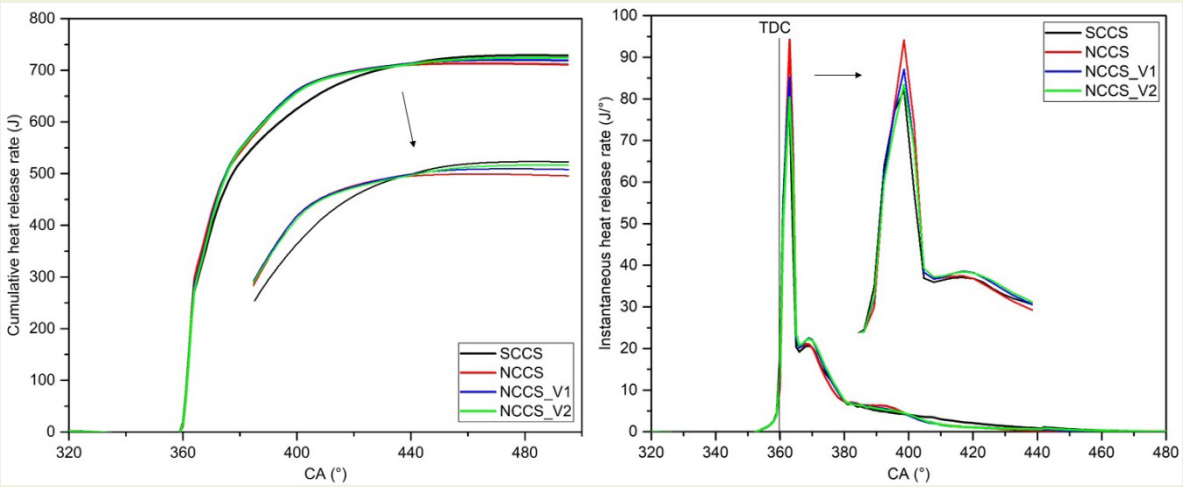

Figure 3. Change of cumulative and instantaneous heat release rates for NCCS and SCCS geometries

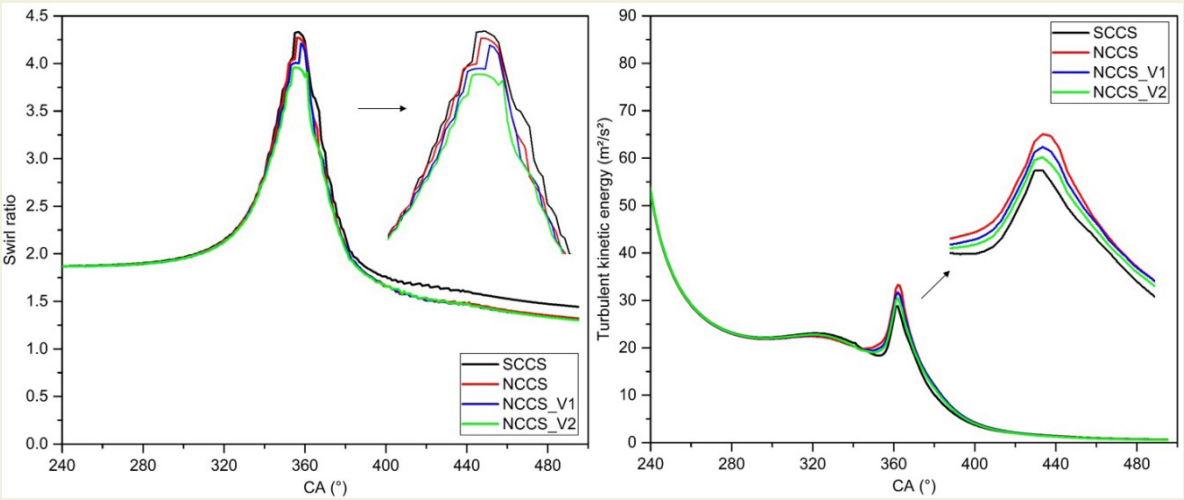

Figure 4. Change of turbulent kinetic energy and swirl ratio with crank angle for NCCS and SCCS geometries

the maximum cylinder temperature and pressures are slightly higher than SCCS (Fig. 2). In these combustion chambers, the increase in in-cylinder temperatures in parallel with the improvement of mixture formation is thought to be the most importance factor in the increase of NO emissions. In NCCS geometries, it can be said that improvement is achieved in other incomplete combustion products (CO, UHC and CO2) other than NO. Plastering the fuel sprayed on the combustion chamber wall may cause the droplets to evaporate in a shorter time by taking advantage of the wall temperature. In the analyzes made for different radius values of the inner wall, it was determined that in particular NO emission decreased depending on the change in the distance in the penetration depth of the fuel. When the exhaust emission (soot, CO and HC) formations in these models were examined, the NCCS compared to the SCCS was determined that there were significant reductions (Fig. 5). The NCCS compared to the SCCS, it is seen that the most reduction in in-cylinder soot (Particular matter) formation occur-

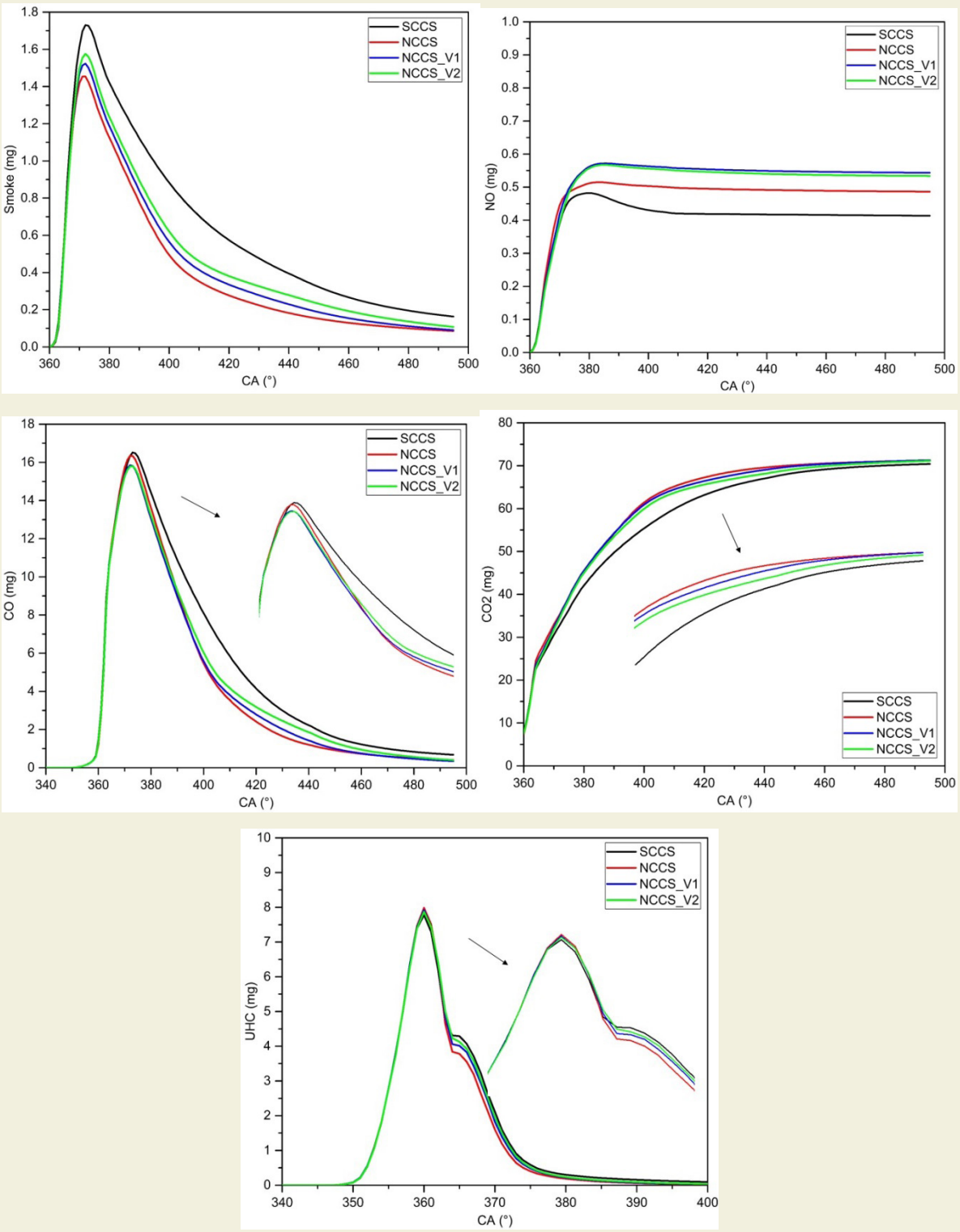

Figure 5. Change of exhaust emission values (Smoke, NO, CO, CO2 and UHC) obtained for NCCS and SCCS geometries

red. According to CFD analyses, the NCCS compared to the SCCS when the amount of soot generated in a cycle at the moment the exhaust valve is opened, a reduction of 40.3% was achieved. Improvement of mixture formation, and wall-fuel interaction is thought to be important in this reduction. As a matter of fact, CO_2 emissions increased in parallel with the improvement of combustion (Fig. 5).

Fig. 6 and Fig. 7 show some analyzes inside the combustion chambers of two different pistons at 720° CA (upper) and 730° (lower) CA. When the temperature/fuel spray distributions are examined, it is seen that the swirl influence in-chamber is important (Fig. 6). Swirl affects the distribution of the fuel droplets in the chamber, the combustion efficiency, and therefore exhaust emissions are affected. Fuel droplets seen in numerical analyzes represent liquid fuel. SCCS seems to be more intense regionally than NCCS (located on the left side of the figure). When the liquid particle distribution of NCCS, which

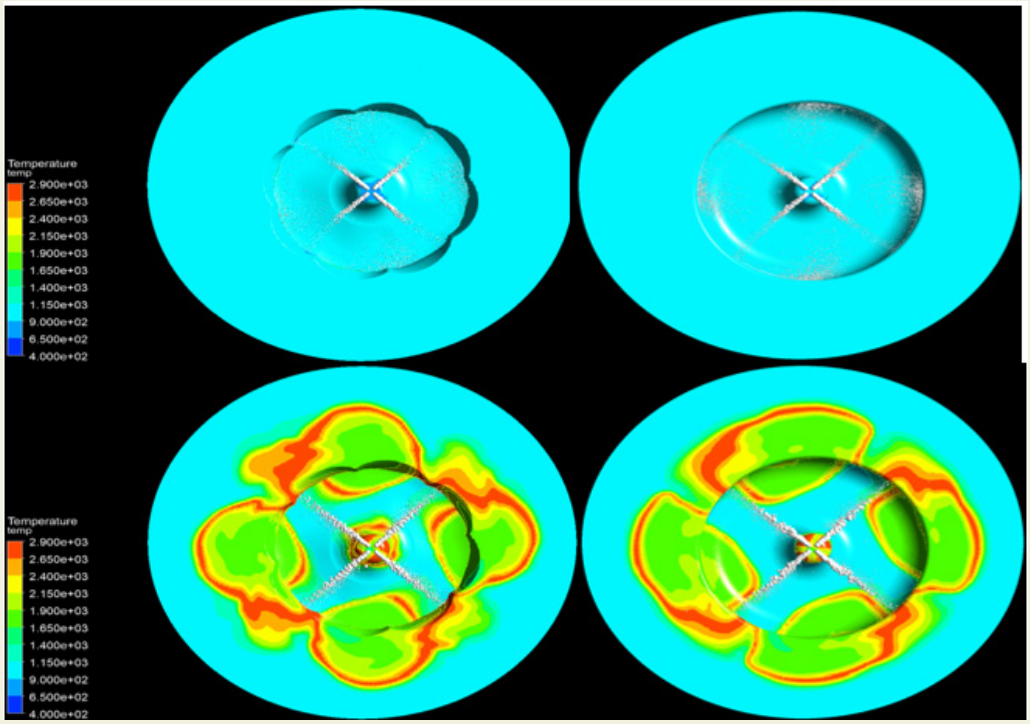

Figure 6. Temperature changes of NCCS and SCCS geometries

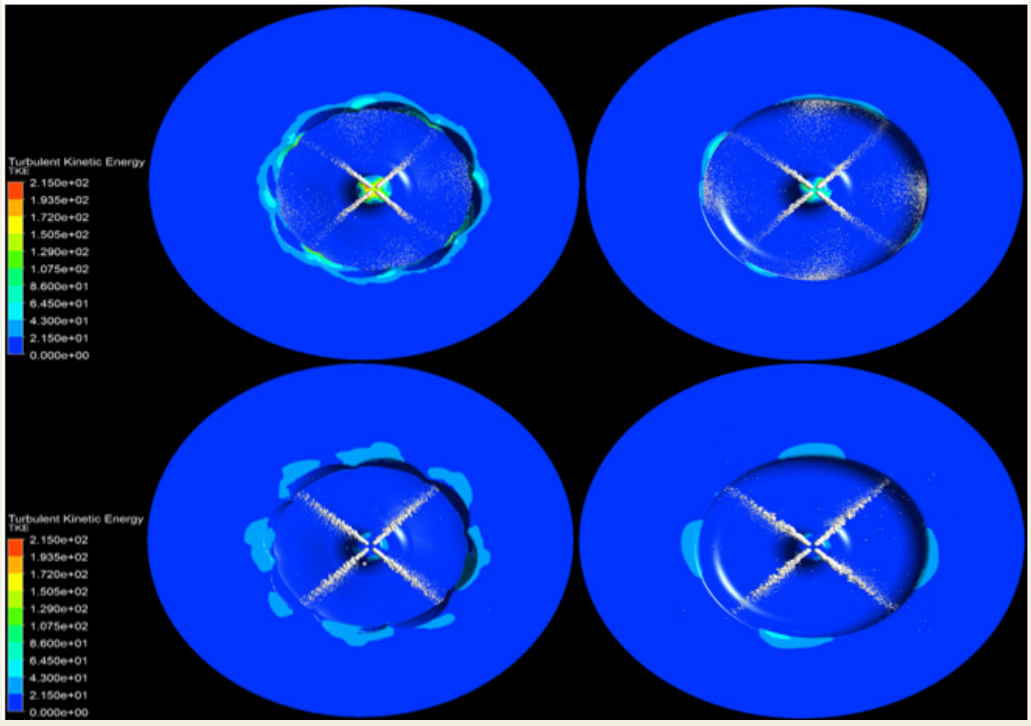

Figure 7. TKE changes of NCCS and SCCS geometries

has eight (8) cavity structures, is examined, a less, and more homogeneous distribution is observed compared to SCCS. This situation is thought to be a result of increasing the evaporation level by taking advantage of the wall temperature of the fuel. An improvement can be seen in the mixture as the amount of steam in the vapor + liquid fuel increases. In addition, some differences in combustion may occur. This is also of great importance in terms of emissions. The energy loss caused by the liquid fuel hitting a flat wall affects the fuel and flame distribution. When the TKE distribution images for different combustion chambers are examined, it can be said that the flow rate is more realized for NCCS geometries (Fig. 7). Although the swirl ratios in the swirl graphs are similar for both combustion chambers, it can be mentioned that the squish mobility is reflected in the TKE (Fig. 7). As a matter of fact, this issue is reflected in the velocity distribution graphs for both crank angles.

Swirl and tumble are called the movements of the air or air/fuel mixture in the chamber. While the swirl movement develops parallel to the cylinder axis, the tumble takes place perpendicular to the movement axis of the piston. Squish movements also produce a tumble flow when the piston reaches the TDC. The dimensionless parameter known as SQ is used to measure squish mobility.

For the squish rate;

$$SQ=A_{squish}/A_{total}$$

In other words, it is the ratio of the top surface area of the piston crown to the cylinder surface area of the total piston. Squish level is determined by the gap between the piston and the head. According to Taylor, the diameter of the gap having a value of less than 0.005 is very important in terms of improvement [20]. The upper surface view of the piston for two different combustion chambers is presented in Fig. 9.

The NCCS compared to the SCCS, an increase in SQ (squish ratio) has been achieved. It can be said that this increase is also reflected in the TKE and velocity distributions obtained in the numerical analysis. Excessive SQ ratio is known to increase knocking tendencies in engines [21]. The absence of such a finding based on the numeri-

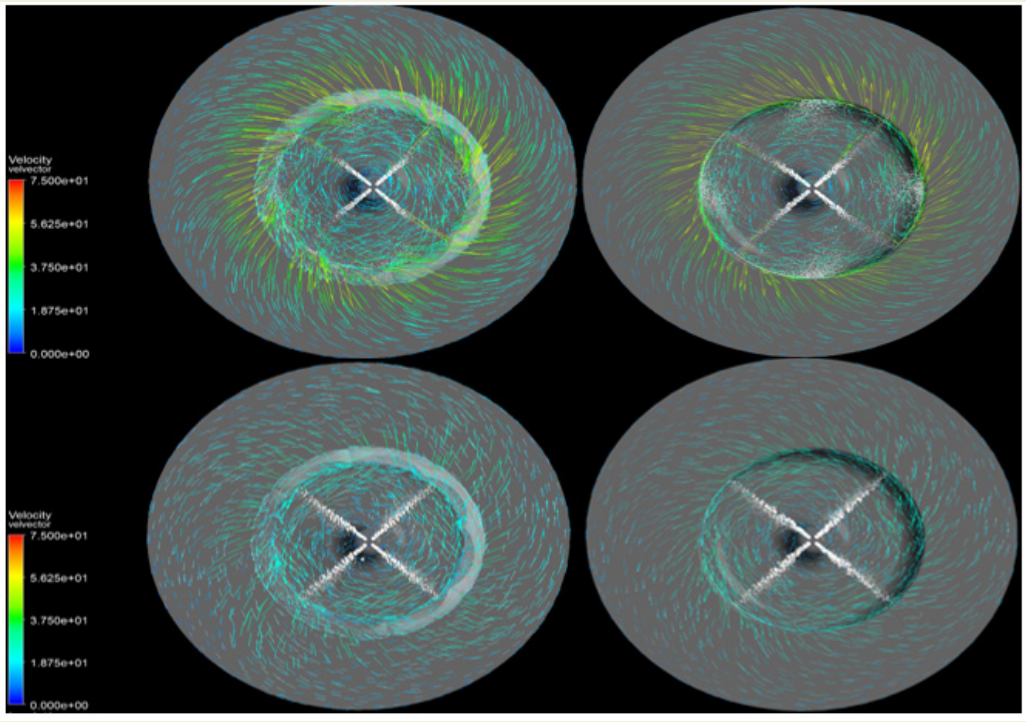

Figure 8. Velocity distributions of NCCS and SCCS geometries

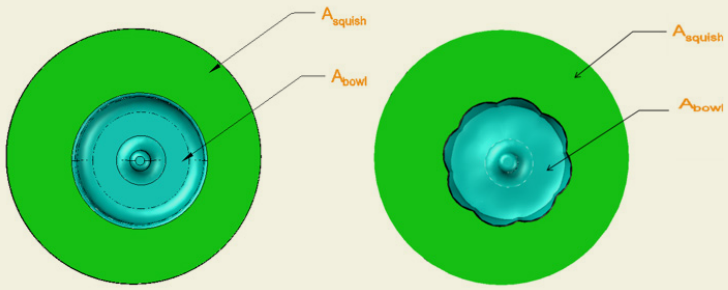

Figure 9. Representation of the upper surface areas of NCCS and SCCS pistons

Table 3. Changes in the surface areas of both pistons

CC Type	A_{squish} (mm^2)	$A_{bowl,top}$ (mm^2)	A_{total} (mm^2)	$A_{bowl,surface}$ (mm^2)	SQ
SCCS	4055.6	1618.9	5674.5	3819	0.71
NCCS	4241	1433.5	5674.5	4020	0.74

cal study data shows that the design is acceptable within the limits of conformity. Another parameter accepted in combustion chamber designs is the "k factor" value. This value is known as the ratio of the bowl volume to the total volume when the piston is in TDC. In order to reveal the effect of geometry in the combustion chamber design, no changes were made in compression ratios and k-factor. Table 3 shows the variation of the bowl surface area in the chamber for two different chamber geometries. Increasing the bowl surface area means that the thermal forces on the piston are reduced, and the amount of heat transfer from the wall increases. It will also mean some improvement in the mixture formation of fuel droplets guided by evaporation through the wall. In many studies, it is emphasized that squish movements around the TDC are effective on turbulence [22-25]. More TKE is occurring as seen in the NCCS. This situation occurred as a result of the effect of squish movements. Looking at the velocity analysis, it can be said that the high flow velocity seen in NCCS developed as a result of the combination of squish and swirl flows. Increasing the flame area increases the heat transfer level of the unburned gas [26]. Due to the increased heat transfer, the increase in the temperature of the unburned gas causes the combustion to take place faster, and more fuel to participate in the combustion event. Increases in swirl ratios in engines can result in increased NO emissions [27]. Therefore, another important parameter in piston design was the in-cylinder swirl change. Considering the effect of the swirl ratio on other emissions, a slightly lower NCCS geometry was preferred compared to the SCCS geometry.

4. CONCLUSIONS

The findings obtained in this study, in which heat, flow and combustion parameters are examined in combustion chambers with different geometric designs, are listed in the following items;

- The formation of different base radii and the change of penetration distance changed the evaporation amounts by taking advantage of the wall temperature of the fuel.
- Maximum pressure values showed parallelism with the increase in TKE and flow rate in the cylinder.
- The NCCS according to the SCCS, although the swirl rates of the new combustion chamber are similar, the increases in squish rates are effective parameters in increasing the speed and TKE.
- - The air movement created by eight (8) cavities in the combustion chamber, and its effect on fuel distribution caused a decrease in exhaust emissions (CO, C, HC), and increased NO emissions.
- The NCCS compared to the standard combustion chamber, the increased surface area of the geometric piston containing eight (8) cavities prevented local temperatures, and caused it to spread over a wider area.
- Increasing the bowl surface area on the piston means that the thermal forces are reduced, and the amount of heat transfer from engine increases. This case has caused its formation to create of new research on piston rings and engine wear.

ACKNOWLEDGMENT

This study was supported by the Scientific and Technological Research Council of Turkey (TUBITAK) within the scope of project 120M143.

NOMENCLATURE

BDC	Bottom dead center
C	Carbon
CA	Crank angle
CC	Combustion chamber
CFD	Computational fluid dynamics
CO	Carbon monoxide
CO2	Carbon dioxide
NCSS	New combustion chamber system geometry
NO	Nitrogen oxide
SCCS	Standard combustion chamber system
SQ	Squish ratio
TDC	Top dead center
TKE	Turbulent kinetic energy
UHC	Unburned hydrocarbon

REFERENCES

[1] Jaichandar, J., Annamalai, K. (2012). Influences of re-entrant combustion chamber geometry on the performance of Pongamia biodiesel in a DI diesel engine. Energy, 44(1): 633-640. https://doi.org/10.1016/j.energy.2012.05.029

[2] Challen, B., Barnescu, R. (1999). Diesel engine reference book. England: Society of Automotive Engineers; Bath Press.

[3] Montajir, R., Tsunemoto, H., Ishitani, H., Minami, T., (2000). Fuel spray Behavior in a small DI Diesel engine: effect of combustion chamber geometry. SAE Technical Paper, 2000-01-0946: 1-12. https://doi.org/10.4271/2000-01-0946.

[4] Kalay, İ. (2011). Investigation of piston bowl in diesel engines, M.Sc thesis, Istanbul Technical University, Institute of science and technology, Istanbul, Turkey.

[5] Varun, Singh, P., Tiwari, S.K., Singh, R., Kumar, N., (2017). Modification in combustion chamber geometry of CI engines for suitability of biodiesel: A review. Renewable and Sustainable Energy Reviews, 79: 1016-1033. https://doi.org/10.1016/j.rser.2017.05.116

[6] Saito, T., Daisho, Y., Uchida, N., Ikeya, N. (1986). Effects of Combustion Chamber Geometry on Diesel Combustion. SAE Technical Paper, 861186: 71-81. https://doi.org/10.4271/861186.

[7] Yaliwal, V.S., Banapurmath, N.R., Gireesh, N.M., Hosmath, R.S., Donateo, T., Tewari, P.G. (2016). Effect of nozzle and combustion chamber geometry on the performance of a diesel engine operated on dual fuel mode using renewable fuels. Renewable Energy, 93: 483-501. https://doi.org/10.1016/j.renene.2016.03.020

[8] Bapu, B.R.R., Saravanakumar, L., Prasad, B.D. (2017). Effects of combustion chamber geometry on combustion characteristics of a DI diesel engine fueled with calophyllum inophyllum methyl ester. Journal of the Energy Institute, 90(1): 82-100, https://doi.org/10.1016/j.joei.2015.10.004

[9] Sener, R., Yangaz, M.U., Gul, M.Z. (2020). Effects of injection strategy and combustion chamber modification on a single-cylinder diesel engine. Fuel, 266: 1-15. https://doi.org/10.1016/j.fuel.2020.117122

[10] Dimitriou, P., Wang, W., Peng, Z. (2015). A piston geometry and n ozzle spray angle investigation in a DI diesel engine by quantifying the air-fuel mixture. International Journal of Spray and Combustion Dynamics, 7(1): 1-24. https://doi.org/10.1260/1756-8277.7.1.1

[11] Sener, R., Ozdemir, M.R., Yangaz, M.U. (2019). Influence of piston bowl geometry on combustion and emission characteristics. Proceedings of the Institution of Mechanical Engineers, Part A: Journal of Power and Energy, 233(5): 576-587. https://doi.org/10.1177/0957650919854637

[12] Lia, X., Chena, Y., Sub, L., Liua, F. (2018). Effects of lateral swirl combustion chamber geometries on the combustion and emission characteristics of DI diesel engines and a matching method for the combustion chamber geometry. Fuel. 224: 644-660. https://doi.org/10.1016/j.fuel.2018.03.063

[13] Shivashimpi, M.M., Alur, S.A., Topannavar, S.N., Dodamani, B.M. (2018). Combined effect of combustion chamber shapes and nozzle geometry on the performance and emission characteristics of C.I. engine operated on Pongamia. Energy, 154: 17-26. https://doi.org/10.1016/j.energy.2018.04.097

[14] Zhang, L., Ueda, T., Takatsuki, T., Yokota, K., (1995). A study of the effects of chamber geometries on flame behavior in a DI Diesel engine. SAE Technical Paper, 952515: 1-9. https://doi.org/10.4271/952515.

[15] Mittal, G., Gwalwanshi, M. (2021). Influence of reentrant piston bowl geometry on combustion in CI engine. Materials Today: Proceedings, 46(20): 11011-11014. https://doi.org/10.1016/j.matpr.2021.02.098

[16] Liu, D., Li, X., Shang, H., Xie, L., Chen, Y., Chang, J. (2021). Combustion performance and fuel injection timing adaptability of a lateral swirl combustion system for direct injection diesel engines. Fuel, 286: 1-15. https://doi.org/10.1016/j.fuel.2021.120663

[17] Temizer, İ., Cihan, Ö., Eskici, B. (2020). Numerical and experimental investigation of the effect of biodiesel/diesel fuel on combustion characteristics in CI engine. Fuel, 270: 1-9. https://doi.org/10.1016/j.fuel.2020.117523

[18] Amate A.P., Khairnar, H.P. (2015). Disquisition on Diesel Engine Emissions and Piston Bowl Parameters. International Advanced Research Journal in Science, Engineering and Technology, 2(7): 42-49. doi: 10.17148/IARJSET.2015.2710

[19] Sreedharan, S.N., Krishnan, R. (2018). Development of tool to design piston bowl considering spray parameters to reduce emissions. Materials Science and Engineering, 396: 1-8: doi:10.1088/1757-899X/396/1/012055.

[20] Kaplan, M. (2019). Influence of swirl, tumble and squish flows on combustion characteristics and emissions in internal combustion engine-review. International Journal of Automotive Engineering and Technologies (IJAET), 8(2): 83-102. https://doi.org/10.18245/ijaet.558258

[21] Towers, J., Hoekstra, R. (1998). Engine knock, A renewed concern in motorsports - A literature review. SAE Technical Paper, 983026: 1-17. https://doi.org/10.4271/983026.

[22] Payri, F., Benajes, J., Margot, X., Gil, A. (2004). CFD modeling of the in-cylinder flow in direct-injection Diesel engines. Computers & Fluids, 33: 995-1021. https://doi.org/10.1016/j.compfluid.2003.09.003

[23] Gunabalan, A., Ramprabhu, R. (2009). Effect of piston bowl geometry on flow, combustion and emission in DI engines-a CFD approach. International Journal of Applied Engineering Research, 4(11): 2181-2188.

[24] Raj, A.R.G.S., Mallikarjuna, J.M., Ganesan, V. (2013). Energy efficient piston configuration for effective air motion – A CFD study. Applied Energy, 102: 347-354. https://doi.org/10.1016/j.apenergy.2012.07.022

[25] Harshavardhan, B., Mallikarjuna, J.M. (2015). Effect of piston shape on in-cylinder flows and air-fuel interaction in a direct injection spark ignition engine - A CFD analysis, Energy, 81: 361-372. https://doi.org/10.1016/j.energy.2014.12.049

[26] He, Y. (2007). Effect of intake primary runner blockages on combustion characteristics and emissions in spark ignition engines, PhD Thesis, University of Ohio, USA.

[27] Genzale, C., Wickman, D., Reitz, R.D. (2006). An advanced optimization methodology for understanding the effects of piston bowl design in late injection low-temperature Diesel combustion, In: Proceedings of THIESEL 2006 conference on "thermo and fluid dynamic processes in diesel engines", Valencia-Spain.

EUROPEAN MECHANICAL SCIENCE

Research Article

e-ISSN: 2587-1110

PEMEC performance evaluation through experimental analysis of operating conditions by response surface methodology (RSM)

Safiye Nur Özdemir[1]*, İmdat Taymaz[1], Emin Okumuş[2], Fatmagül Boyacı San[2]

[1]Sakarya University, Faculty of Engineering, Mechanical Engineering Department, Sakarya, Turkey
[2]Energy Institute, Tubitak Marmara Research Center, Gebze, Kocaeli, Turkey

ORCID: S.n. Özdemir (0000-0003-1337-7299), İ. Taymaz (0000-0001-5025-5480), E. Okumuş (0000-0003-1132-7052), F. Boyaci San (0000-0002-5578-1145)

Abstract: The optimum current value of the proton exchange membrane electrolysis cell (PEM-EC) mainly depends on various operational factors, such as temperature, operating pressure, water flow rate, and membrane water content. Therefore, this study aims to maximize performance related to the current of PEM-EC by determining the optimal operating conditions of the PEM electrolysis cell having a 9 cm² active layer. In this regard, response surface methodology (RSM) and central composite design (CCD) were applied using Design-Expert (trial version) software to identify the optimal combination of operating variables such as temperature, pump speed, and cell voltage. Temperature, pump speed, and cell voltage were the independent variables to have ranged from 40-80 °C, 1-8, and 1.8-2.3 V, respectively. Also, the individual and combined effects of operational parameters on cell performance will be included in this study by ANOVA (analysis of variance). The optimal parameters are 80 °C, 1, and 2.3 V, respectively, temperature, pump speed, and cell voltage corresponding to the maximum current output of PEM-EC. This RSM tool found that the maximum current was 16.778 A. In addition, it was concluded that the most influential parameter on cell performance was the cell voltage, followed by the temperature.

Keywords: PEM electrolysis cell, Operational conditions, Optimization, Response surface methodology (RSM)

1. INTRODUCTION

Most research on renewable energy technologies became a widespread issue last decades due to the rapid depletion of fossil resources, the negative impact of conventional fossil fuel-based energy sources on human health and the environment, and fluctuations in natural gas or oil prices. The most crucial property of renewable energy sources is their environment friendly. Hydrogen will soon become one of the cleanest, non-toxic, and most sustainable energy carriers with this feature. Low-polluting and high-purity hydrogen and oxygen can be produced from water electrolysis compared with traditional hydrogen production methods such as alkaline water electrolysis, ammonia cracking, and fossil fuel reforming [1-3]. Hydrogen and oxygen from water electrolysis can be used directly in fuel cells and industrial applications. Additionally, water electrolysis utilizes DC power from renewable energy sources such as wind, solar, and geothermal. The cost of hydrogen production may differ depending on the renewable and nuclear energy sources used for water electrolysis. Compared to other renewable energy sources (geothermal, nuclear, and wind), solar energy has the highest cost, ranging from 10 to 30 $/kg [4].

The performance and durability of the PEM electrolysis system have been dependent on the design and operating parameters, membrane, and electrode characteristics. With the increasing demand for green hydrogen, the PEM electrolysis cell has become a trending topic in recent years. However, due to the low hydrogen production rate and high energy consumption, the efficiency of the PEM electrolysis cell remains low in terms of economic competitiveness. Therefore, many studies have been conducted to enhance efficiency and cell performance. Mass transport losses at high current densities are essential in reducing efficiency [5-7]. According to Faraday's law, oxygen gas production increases at the anode electrode of the PEM electrolysis cell at high current densities. The formation of oxygen bubbles over time interferes with the electrolysis reaction of water in the anode catalyst layer, which degrades PEM electrolysis cell performance [8]. The physical properties of the porous transport layer, such as the thickness and pore size, must be controlled to minimize mass transport limitations. Many studies have also been conducted to examine the performance of PEM electrolysis at low current densities (about 2 A/cm²) to reduce mass transport loss, such as [9-10]. To increase

* Corresponding author.
Email: safiyeozdemir@sakarya.edu.tr

European Mechanical Science (2023), 7(1): 16-21
https://doi.org/10.26701/ems.1203924
Received: November 14, 2022 — Accepted: January 13, 2023

the performance of the PEM electrolysis cell, voltage losses must be minimized. Afshari et al. [11] proposed a zero-dimensional mathematical model to investigate voltage losses. The results indicated that the activation over-potential contributes the highest to the cell voltage, while the concentration over-potential contributes the lowest. Therefore, activation and ohmic over-potentials need to be decreased to boost the performance of PEM electrolysis cells. Temperature, pressure, and water flow rate are the operating conditions that significantly affect the performance of the PEM electrolysis cell. Santarelli et al. [12] conducted performance tests of a 160 cm^2 active area PEM electrolyzer stack. They found that decreasing the water temperature or increasing the cathode pressure can reduce efficiency. At the maximum electrical power supplied to the PEM electrolysis cell, the power difference between the best (700 kPa, 58 °C) and worst (7000 kPa, 42 °C) conditions was approximately 0.5 kW. Upadhyay et al. [13] developed a steady, three-dimensional computational fluid dynamics (CFD) model. They discovered that the best water temperature range of the PEM electrolysis stack is 40 °C-80° C. Increasing the cathode pressure augmented the demand for electrical input power, which decreased cell performance. Numerical results showed that low gas diffusion layer porosity and water flow rate require high power. Lin et al. [14] numerically compared the parallel, triple-serpentine, and pin flow field configurations. They found that compared to other flow field designs, the best cell performance is obtained in the parallel flow field plate due to its good mass transfer, uniform pressure distribution, and low contact impedance characteristics. As a result of orthogonal experiments, the flow field design most affected the PEM electrolysis performance. Lee et al. [15] optimized the working conditions of the PEM electrolysis cell to improve its efficiency and performance PEMEC. Their study investigated sulfuric acid flow, direction, and flow rate in the anode and cathode compartments of the PEM-EC, catalyst coating, and various catalytic materials. Lickert et al. [16] examined the impacts of temperature, pressure, and water flow rate on cell performance on two stacks of PEM electrolyzers, one with the flow field in the anode chamber and the other without the flow field arrangement. It was concluded that the operating conditions have a crucial effect on the polarization performance of the PEM electrolyzer stack, which has no flow field design under the porous transport layer. In addition, it was observed that the mass transfer loss decreased with increasing temperature, pressure, and water flow rate. Although many numerical and experimental studies have been conducted in the literature to improve the efficiency of PEM electrolysis cells, the current research in which the design or operating parameters affecting the cell performance were optimized with an optimization tool has been carried out in the last few years. This study investigated the effects of temperature, water feed rate or pump speed, and cell voltage on cell performance by experimental design. In addition, the optimization of input factors for high current values based on response surface methodology (RSM) has been brought to the literature.

2. MATERIAL AND METHOD

The performance tests of single-cell PEM-EC with an active area of 9 cm^2 were carried out in the experimental test setup in the TUBITAK MAM Energy Institute laboratory. The main components of the experimental test bench consisted of a PEM-EC, Heidolph heater, TDK-Lambda DC power supply (760 W), ENDA temperature controller, Masterflex peristaltic pump, and a data acquisition system (see Figure 1). Design-of-experiment (DOE) and RSM are excellent tools to reveal the objective function's optimum value and minimize the number of experiments. Applying the RSM method to the experimental system reduces the number of experimental trials and saves time and cost. The RSM method reveals the response-input parameter relationship with three-dimensional contour plots. It combines strategy and experimental designs to create a novel data set with first or second-order polynomial equations. RSM is a mathematical and statistical tool that describes the effects, contributions, and interactions between independent variables on the dependent variable. In this study, temperature, pump speed, and cell voltage are independent variables. Current is the dependent variable. To investigate the effect of input factors on the output factors in the region of investigation, a central composite design (CCD) was applied using Design-Expert (trial version). CCD fits the second-order response surface, including axial point runs, center point runs, and cube point runs. The total number of experiments with three variables is 17. This paper's response surface consists of a second-order model with a minor numerical error (see Equation 1).

$$y = \beta_0 + \sum_{i=1}^{3} \beta_i X_i + \sum_{i=1}^{3} \beta_{ii} X_i^{\,2} + \sum_{i=1}^{3} \sum_{j=i+1}^{3} \beta_{ij} X_i X_j + e$$

Where y is the predicted response (current and hydrogen flow rate), β_0 is the constant coefficient, X_i ($i = 1-3$) is the main factor, β_i is the linear term, β_{ii} is the quadratic term, and β_{ij} ($i\,and\,j = 1-3$) is the second-order interaction coefficient.

3. RESULTS AND DISCUSSION

This study optimized operating conditions using the CCD and the RSM to obtain the maximum current value. The effects of temperature (A), pump speed (B), and cell voltage (C) on the response (current) in the PEM electrolysis cell were analyzed in Design-Expert (trial-version) software. The RSM tool used low and high values of each input factor to identify significant parameters, as seen in Table 1. Analysis of variance (ANOVA) was employed for the central composite experiment design. ANOVA results of responses affected by operating conditions are given in Table 2. If p-values are greater than 0.1000, the model term is insignificant; if less than 0.0500, the model term is significant. In this case, cell temperature (A), cell voltage (C), and cell temperature-cell voltage (AC) were considerable model terms for current. The Pred R^2 of 0.9944 good agreed with the Adj R^2 of 0.9989 since the

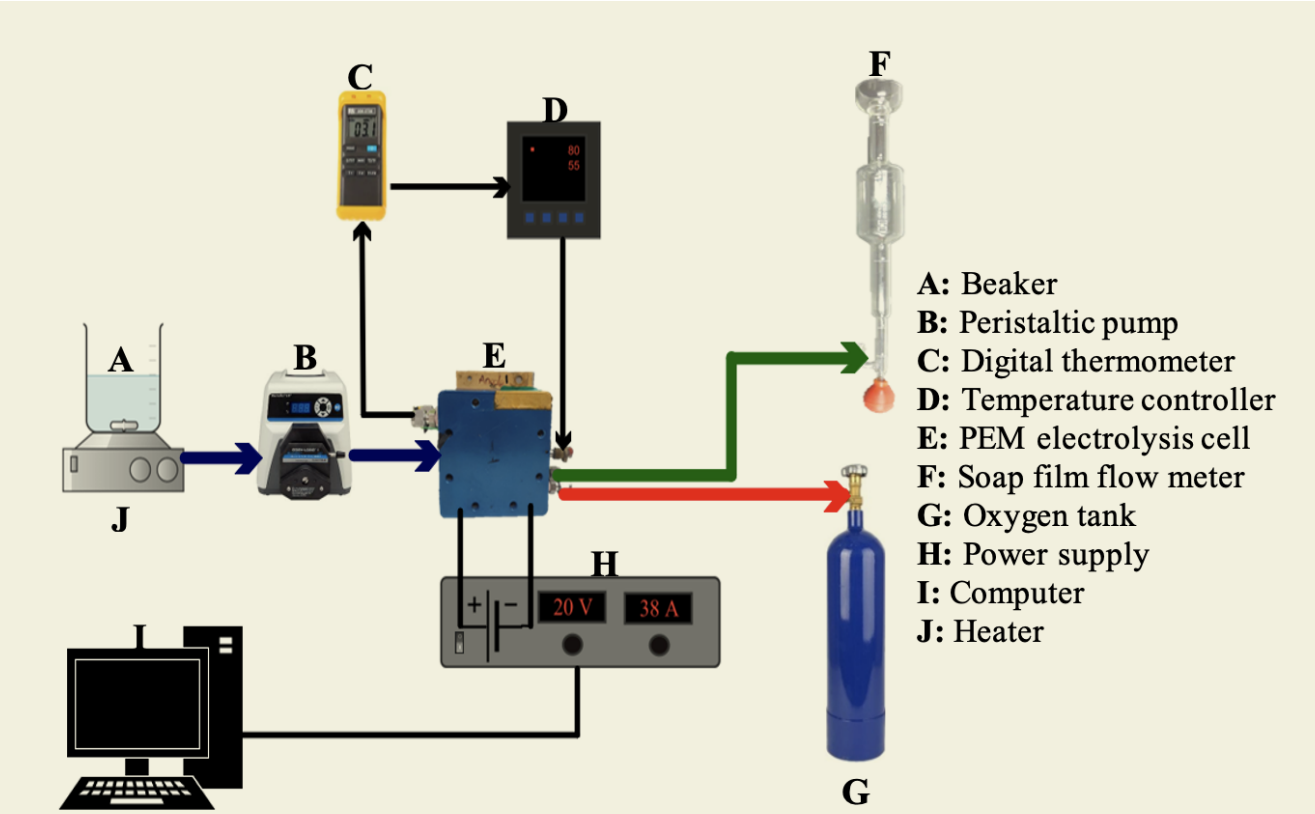

Figure 1. Experimental setup

difference between them is much smaller than 0.2. The regression analysis was carried out in Design-Expert (trial version), and the regression analysis of the input factors is given in a quadratic equation as follows:

Figure 2 (a-c) illustrates the interrelationships between temperature and pump speed (a), temperature and cell voltage (b), and pump speed and cell voltage (c) on current. The most influential parameter on cell performance is voltage, followed by temperature and pump speed, respectively. PEM-EC performance improves with an increase in cell voltage and temperature. On the other hand, operating temperatures above 80 °C cause damage to the membrane, which negatively affects cell perfor-

Table 1. Design table of experiments

Std order	Run	Factor 1 Temperature (°C)	Factor 2 Pump Speed	Factor 3 Cell Voltage (V)	Response 1 Current (A)
14	1	60	4	2.3	14.72
4	2	80	8	1.8	3.48
9	3	40	4	2	6.52
17	4	60	4	2	7.46
7	5	40	8	2.3	12.58
6	6	80	1	2.3	16.77
3	7	40	8	1.8	2.72
2	8	80	1	1.8	3.83
10	9	80	4	2	8.2
12	10	60	8	2	7.37
11	11	60	1	2	7.55
1	12	40	1	1.8	2.54
8	13	80	8	2.3	16.6
15	14	60	4	2	7.48
5	15	40	1	2.3	12.8
13	16	60	4	1.8	3.3
16	17	60	4	2	7.5

Table 2. ANOVA results for current

Source	Sum of Squares	df	Mean Square	F-value	p-value
Model	359.39	9	39.93	1632.67	<0.0001
A: Cell temperature (°C)	14.37	1	14.37	587.64	<0.0001
B: Pump speed	0.0561	1	0.0561	2.29	0.1736
C: Cell voltage (V)	331.36	1	331.36	13548.07	<0.0001
AB	0.0219	1	0.0219	0.8961	0.3754
AC	4.58	1	4.58	187.12	<0.0001
BC	0.0049	1	0.0049	0.1997	0.6684
Residual	0.1712	7	0.0245		
Lack of fit	0.1704	5	0.0341	85.20	0.0116
Pure error	0.0008	2	0.0004		
Cor Total	359.56	16			
Standard deviation	0.1564			R^2	0.9995
Mean	8.32			Adj R^2	0.9989
C.V.%	1.88			Pred R^2	0.9944

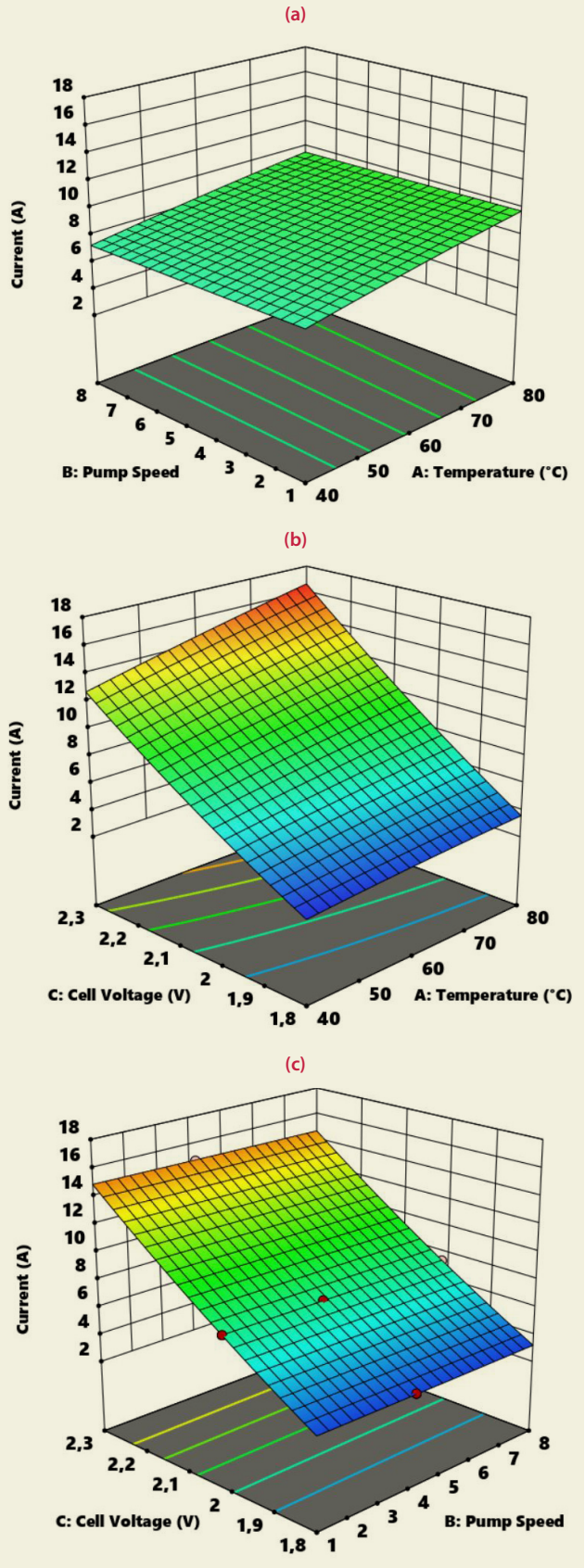

Figure 2. Current as a function of temperature and pump speed (a), temperature and cell voltage (b), pump speed and cell voltage (c)

mance. Variation in pump speed had no crucial effect on the performance of the PEM-EC.

At the end of this experimental study, optimum operating conditions for maximum cell performance were found. In the optimization process, we maximize the current and ensure that the control or input factors remain within the specified range (see Table 3). The importance and weight values of the input and output factors are given in Table 3. Optimum points with a desirability value greater than 0.995 are shown in Table 4. Maximum current (16.778 A) was obtained with a cell temperature

Table 3. Optimization for maximum current

Variable	Goal	Lower limit	Upper limit	Lower weight	Upper weight	Importance
Temperature (°C)	is in range	40	80	1	1	3
Pump speed	is in range	1	8	1	1	3
Cell voltage (V)	is in range	1.8	2.3	1	1	3
Current (A)	maximize	2.54	16.77	1	1	5

Table 4. Optimized results

Run	A: Temperature (°C)	B: Pump speed	C: Cell voltage (V)	R1: Current (A)	Desirability
1	80.000	1.000	2.300	16.778	1.000
2	79.997	1.042	2.300	16.773	1.000
3	79.966	1.068	2.300	16.772	1.000
4	80.000	1.637	2.300	16.748	0.999
5	79.603	1.000	2.300	16.742	0.999
6	80.000	1.687	2.300	16.745	0.999
7	80.000	1.755	2.300	16.742	0.998
8	79.136	1.034	2.300	16.699	0.997
9	80.000	2.242	2.300	16.719	0.996
10	80.000	2.332	2.300	16.715	0.995

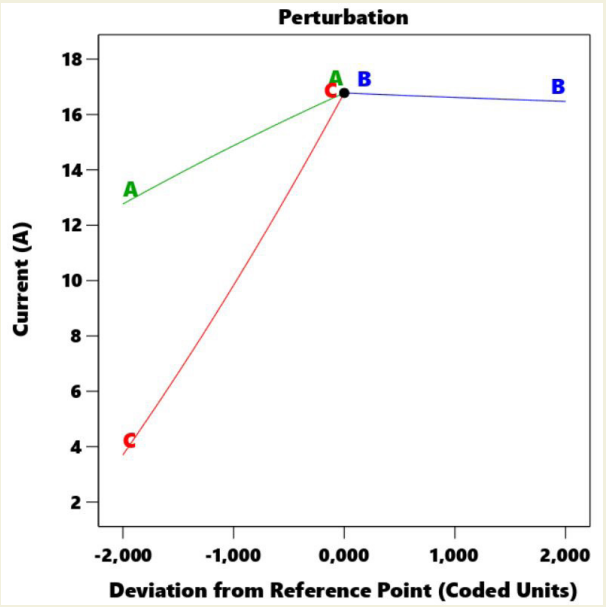

Figure 4. The perturbation plot for current

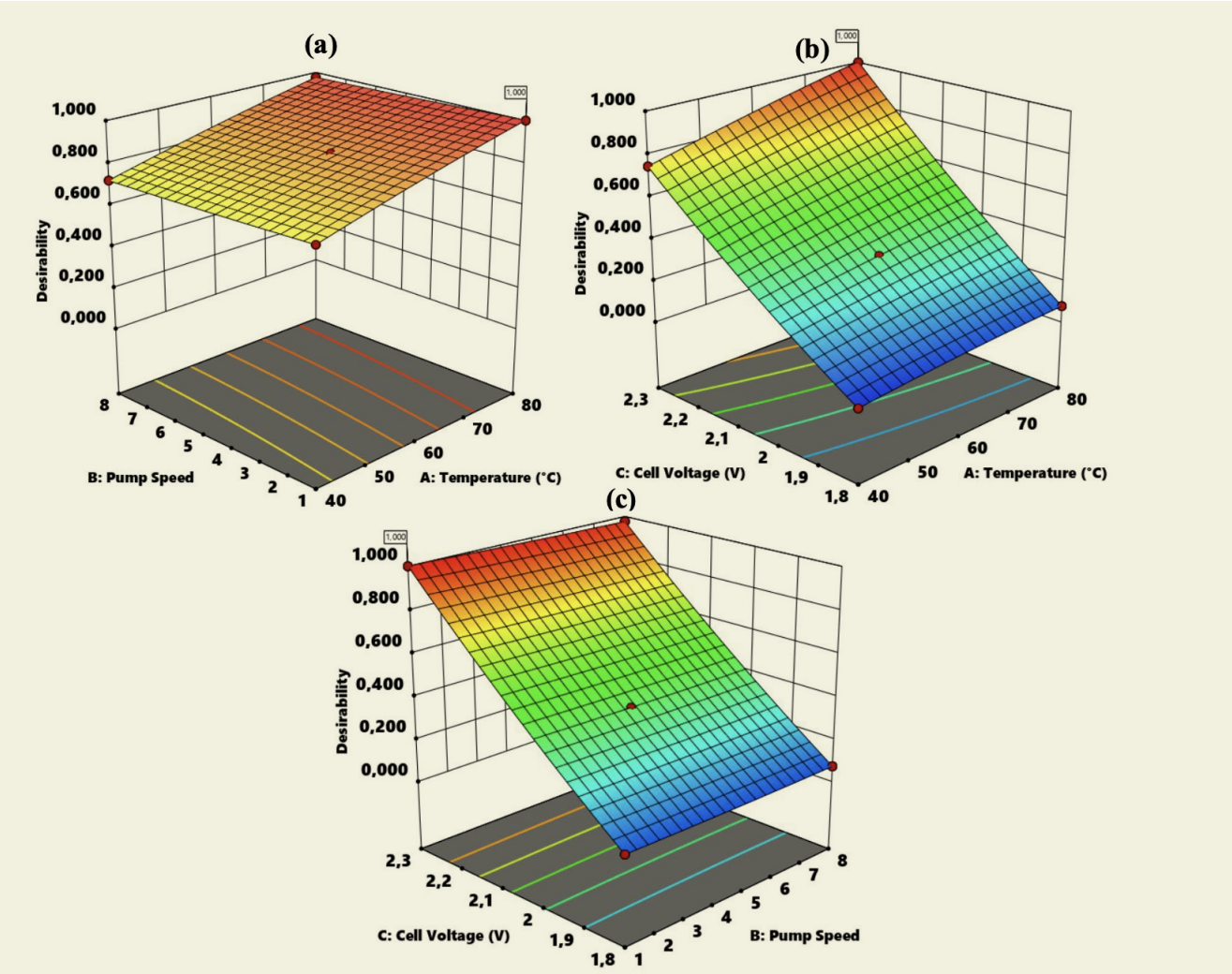

Figure 3. The desirability plots as a function of temperature and pump speed (a), temperature and cell voltage (b), pump speed and cell voltage (c)

of 80 °C, pump speed of 1, and cell voltage of 2.3 V. Figure 3 shows the desirability plots as a function of control factors. The excellent agreement of the experimental and optimization results and the high desirability value show that a reliable and accurate model has been developed. The intersection point of the operating conditions shows the optimum point and is shown on the perturbation plot (see Figure 4). The cell voltage has the steepest slope compared to the others, which means it is the most influential factor on the current.

4. CONCLUSIONS

The performance tests of a PEM-EC having a 9 cm^2 active area layer under different operational conditions have been conducted to investigate the influences of temperature, pump speed or water flow rate, and cell voltage on the cell performance. The central-composite design (CCD) and response surface methodology (RSM) were used to identify the optimal operating conditions for boosting the output current. It was concluded that the main factors affecting the performance of the PEM-EC are the cell voltage and temperature. On the other hand, the increase in pump speed did not have a significant effect on cell performance. The rise in temperature and cell voltage accelerates the electrolysis of water, and the formation of oxygen bubbles in the PEM electrolysis cell increases, so the evacuation of oxygen bubbles from the outside of the cell is provided with a low pump speed. The maximum current value of 16.778 A was obtained at 80 °C, pump speed of 1, and cell voltage of 2.3 V.

ACKNOWLEDGEMENTS

This study was supported by the Scientific and Technological Research Council of Turkey (TUBITAK, PN: 5212A01) and the Turkish Energy, Nuclear, and Mineral Research Agency (TENMAK).

REFERENCES

[1] Grigoriev, S., Porembsky, V., Fateev, V. (2006). Pure hydrogen production by PEM electrolysis for hydrogen energy. International Journal of Hydrogen Energy, 31(2):171–175, https://doi.org/10.1016/j.ijhydene.2005.04.038

[2] Shiva Kumar, S., Himabindu, V. (2019). Hydrogen production by PEM water electrolysis – A review. In Materials Science for Energy Technologies, 2(3):442-454, https://doi.org/10.1016/j.

mset.2019.03.002

[3] Ruiz Diaz, D., Valenzuela, E., Wang, Y. (2022). A component-level model of polymer electrolyte membrane electrolysis cells for hydrogen production. Applied Energy, 321:119398, https://doi.org/10.1016/j.apenergy.2022.119398

[4] Yilmaz, C., Kanoglu, M. (2014). Thermodynamic evaluation of geothermal energy powered hydrogen production by PEM water electrolysis. Energy, 69:592–602, https://doi.org/10.1016/j.energy.2014.03.054

[5] Garcia-Navarro, J., Schulze, M., Friedrich, K. (2019). Measuring and modeling mass transport losses in proton exchange membrane water electrolyzers using electrochemical impedance spectroscopy. Journal of Power Sources, 431:189–204, https://doi.org/10.1016/j.jpowsour.2019.05.027

[6] Grigoriev, S., Kalinnikov, A., Millet, P., Porembsky, V., Fateev, V. (2010). Mathematical modeling of high-pressure PEM water electrolysis. Journal of Applied Electrochemistry, 40(5):921–932, https://doi.org/10.1007/s10800-009-0031-z

[7] Parra-Restrepo, J., Bligny, R., Dillet, J., Didierjean, S., Stemmelen, D., Moyne, C., Degiovanni, A., Maranzana, G. (2020). Influence of the porous transport layer properties on the mass and charge transfer in a segmented PEM electrolyzer. International Journal of Hydrogen Energy, 45(15):8094–8106, https://doi.org/10.1016/j.ijhydene.2020.01.100

[8] Peng, L., Wei, Z. (2020). Catalyst Engineering for Electrochemical Energy Conversion from Water to Water: Water Electrolysis and the Hydrogen Fuel Cell. In Engineering, 6(6):653–679, https://doi.org/10.1016/j.eng.2019.07.028

[9] Liso, V., Savoia, G., Araya, S., Cinti, G., Kær, S. (2018). Modelling and experimental analysis of a polymer electrolyte membrane water electrolysis cell at different operating temperatures. Energies, 11(12), https://doi.org/10.3390/en11123273

[10] Abdin, Z., Webb, C., Gray, E. (2015). Modelling and simulation of a proton exchange membrane (PEM) electrolyser cell. International Journal of Hydrogen Energy, 40(39):13243–13257. https://doi.org/10.1016/j.ijhydene.2015.07.129

[11] Afshari, E., Khodabakhsh, S., Jahantigh, N., Toghyani, S. (2021). Performance assessment of gas crossover phenomenon and water transport mechanism in high pressure PEM electrolyzer. International Journal of Hydrogen Energy, 46(19):11029–11040. https://doi.org/10.1016/j.ijhydene.2020.10.180

[12] Santarelli, M., Medina, P., Calì, M. (2009). Fitting regression model and experimental validation for a high-pressure PEM electrolyzer. International Journal of Hydrogen Energy, 34(6):2519–2530. https://doi.org/10.1016/j.ijhydene.2008.11.036

[13] Upadhyay, M., Kim, A., Paramanantham, S., Kim, H., Lim, D., Lee, S., Moon, S., Lim, H. (2022). Three-dimensional CFD simulation of proton exchange membrane water electrolyser: Performance assessment under different condition. Applied Energy, 306(PA):118016, https://doi.org/10.1016/j.apenergy.2021.118016

[14] Lin, R., Lu, Y., Xu, J., Huo, J., Cai, X. (2022). Investigation on performance of proton exchange membrane electrolyzer with different flow field structures. Applied Energy, 326:120011, https://doi.org/10.1016/j.apenergy.2022.120011

[15] Lee, H., Yesuraj, J., Kim, K. (2022). Parametric study to optimize proton exchange membrane electrolyzer cells. Applied Energy, 314:118928, https://doi.org/10.1016/j.apenergy.2022.118928

[16] Lickert, T., Kiermaier, M., Bromberger, K., Ghinaiya, J., Metz, S., Fallisch, A., Smolinka, T. (2020). On the influence of the anodic porous transport layer on PEM electrolysis performance at high current densities. International Journal of Hydrogen Energy, 45(11):6047–6058. https://doi.org/10.1016/j.ijhydene.2019.12.204

EUROPEAN MECHANICAL SCIENCE

Research Article

e-ISSN: 2587-1110

Cylindrical cam mechanism design with visual basic

Onur Güven[1*], Bedrettin Hakan Karaaslan[2], Ahmet Çakan[3] , Suat Özer[4]

[1] Mersin University, Faculty of Engineering, Department of Mechanical Engineering, Mersin, Turkey
[2] Mersin University, Institute of science, Mersin, Turkey
[3] Mersin University, Faculty of Engineering, Department of Mechanical Engineering, Mersin, Turkey
[4] Manufacturing of Cukurova Machinery and Company., Tarsus, Mersin, Turkey

ORCID: O. Güven (0000-0002-8101-4871), B.H. Karaaslan (0000-0002-6201-3064), A. Çakan (0000-0002-7394-1499), S. Özer (0000-0003-2832-6224)

Abstract: One of the technology products that have taken an important place in our lives from the past to the present is power and motion transfer elements. Power and motion transfer elements are very important for users in terms of facilitating work transfer, easing the workload based on people and ergonomics. One of the basic building blocks of these transmission systems is cam mechanisms. Cam mechanisms consisting mainly of followers and cams; It performs a complementary task by transmitting the follower's movement to the cam assembly by direct contact. While cam mechanisms lighten the work load, it is a frequently preferred system because it takes up little space and contains few parts and allows for a wide range of movements. However, sensitivity to vibration and sudden shock effects and cost problems have led to the development of manufacturing methods of cam mechanisms. In this master's thesis, design and mathematical information about cam mechanisms and cylindrical cam mechanisms are given, and the design of a cylindrical cam mechanism with a vertical multiple output limb was carried out using computer-aided drawing programs Solidworks and Autocad. The use of multiple output limb cam mechanisms is increasing day by day in terms of the width of the work area and the possibility to work with other machines. For this reason, this work is intended to be a guide resource for the reader in industry and science for both cam mechanisms and cylindrical cam mechanisms. Microsoft Excel and Visual Basic programs were used in the calculations and designs, and the design details of the mechanism were revealed with the data and formulas entered into the program.

Keywords: Cam, mechanism, cylindrical cam mechanism, multiple exit limb, cam mechanisms.

1. INTRODUCTION

Cam mechanisms are composed of a follower and a cam. The mechanism transfers the movement of the running unit to the cam system by direct contact. This type of systems have less parts and so occupies less space than the other mechanisms. Considering the simplicity of the system and the significant advantages it provides; cam mechanisms are quite important. One of the most important features of these mechanisms, which facilitate the workload ergonomically and so provides work transfer, is their enabling various types of movements [1-3]. Many movements which are hard to make with other machines and mechanisms become possible with the cam mechanisms flexible way of operation. In the design phase, these circumstances should be taken into consideration and the designs should avoid the problems caused by the dynamic forces and also the sudden shock forces. It is crucial to make the design precisely with minimum error. It should be kept in mind that a possible error in the design will negatively affect the operation of the whole mechanism. The design of the mechanism, the force analysis and the operation of the systems are based on the cam and formed according to the shape of the cam[4-6]. Cam mechanism can be classified based on the positive drive status applied to the follower or on the applied spring load[7-9].

Today, cam mechanisms are used in automotive sector (valve mechanisms), printing presses (punching and taking the papers in), sewing machines (zig zag stitch), toys manufacturing, food production (filling and packing, poultry internal emptying), looms (making patterns) and many other fields where power and motion transfer is required [10-12].

2. USING EXCEL AND AUTOCAD AS AN ALTERNATIVE DESIGN METHOD

Today in engineering, besides the computer-aided design software Solidwords, various other computer design programs like Autocad and Catia are also used. In this chapter, in order to lead/guide the designers who wish

* Corresponding author.
Email: oguvenonur@gmail.com

European Mechanical Science (2023), 7(1): 22-28
https://doi.org/10.26701/ems.1215153
Received: December 8, 2022 — Accepted: February 3, 2023

to use different methods, the design types which can be made by using Microsoft Excel and Autocad together will be discussed. In these Excel-Autocad works, the sample designs for both 200 mm and 300 mm radiused systems have been made.

A 2-D design was made by co-using Excel-Visual Basic-Autocad for a mechanism with a cylindirical cam with 300 mm radius. For the system with 200 mm radius, Excel free data values were integrated in tables and transferred directly into the Autocad's command line, and the design was made through the points.

2.1. Using Visual Basic for Cylindirical Cam Design

In recent years, computer programming languages have been being frequently used in designing 2-D and 3-D models. With their suitability of using computer aided drawing and spreadsheet softwares simultaneously, programming languages provides the users with advantages. These programming languages give the designer the chance to draw the designed form automatically on drawing softwares with the help of the codes written in the system modules. At this point, it is ultimately important the codes to be written and be processed correctly. Because, any minor mistakes may cause the system to malfunction and hence will yield no result.

Among the programming languases, Visual Basic is one of the most frequently used along with drawing softwares. Visual Basic for Applications (VBA) give the users the opportunity to work with numerous interfaces like Excel, Autocad, Solidworks etc. together. By their libraries inserted into the VBA, all operations in the aforementioned interfaces can easily be done on VBA as well.

In this section, the designs of the cylindirical cam mechanism with 200 mm radius, which was discussed in the previous chapters, were made by using VBA, Excel and Autocad. As it can be seen in the designs occured, when the coding is done correctly, the 2-D and 3-D models designs can be made much more easily by use of VBA. VBA interface can be accessed via ''Developer'' tab in Microsoft Excel. In the VBA window opened, the page name on the left is right-clicked and then by clicking ''insert'', VBA's code screen can be reached and new modules can be inserted.

In Aotucad, VBA interface can be accessed via ''Tools'' tab. Under this tab, the user can view the design codes or can directly shift to the VBA module as well. In VBA, system starts with the insertion of the module where the codes to be written in just like Excel. The first difference of using VBA with Autocad than using with Excel is the library. In using VBA on Excel, for the drawings to be transferred into Autocad, the users need to activate the Autocad library by clicking ''Refarences'' button under the ''Tools'' tab in the VBA screen. Otherwise, the system coded in Excel-VBA can not be transferred into Autocad. Another point to be considered while using Autocad and VBA is that although VBA was already installed in Autocad in the past, today this feature is not active/valid anymore. Therefore, VBA is readily installed in the old versions of Autocad. On the other hand, in the new versions, the Autodesk company provides free access to the VBA modules on their web site. The users can download the VBA modules they require from the official web site. Although the Autodesk company tries to eliminate the problem this way, there can be differences between the codes in the integrated and non-integrated VBA modules. The users should take this special situation into consideration.

In this section, in order to demonstrate how the designs are made by VBA-Excel and VBA-Autocad, VBA-based designs were studied both on Excel and on Autocad. To form the groove profile of the cylindirical cam mechanism in the system, the design was made on Autocad 2018 computer-aided drawing software using the codes written on VBA with the X,Y,Z coordinates and radius values which were transferred into Excel. Furthermore, in order to show the operations made on the VBA module through Autocad, Autocad 2006 version, in which the VBA module is integrated in the system, was used. In this design, the form, shown in Fig.1 was resulted by transfering the Rx, Ry and Rz point values (calculated under the previous sections), which were given in Table 1 for the cylinder profile and in Table 2 for the groove profile of the 200 mm cylindirical cam that is moving with 1.047 rad/s.

The profile of the follower's route of the 200 mm radiused cylindirical cam mechanism, which ascends for 1 second and descends for 1 seconds during it's 6 seconds motion, is as shown Figure 1. The coordinate values in the system were transferred into an Excel table in round figures. To facilitate the user's work, in the table in Figure 2., ''Create Drawing'' and ''Clean Table'' buttons were inserted in the code in the VBA module.

With the VBA macro defined for ''Create Drawing'' button, the drawing shown above was automatically created in Autocad when the button is pressed. In order the new coordinate values to be inserted in the table, ''Clean Table'' button was added. Lastly, when the drawing is succesfully generated with this system, the completion of drawing is reported, with the created codes, as shown in the Figure 2 . The codes written in the VBA module are given in Table 3 and Table 4.

In the second stage of the design, the 200 mm radiu-

Table 1. Values obtained upon variables of cylindirical cam mechanisms

Cylindirical Cam Radius, r [mm]	Follower's Linear Speed [m/s]	Cam's Angular Speed [rad/s]	Pressure Angle [°]
150	0.110	1.047	6
200	0.146	1.047	7.93
250	0.182	1.047	9.86
200	0.146	0.524	15.68
200	0.146	1.570	5.35

Table 2. Variable values obtained for 200 mm radiused cylindirical cam

A	B	C	D	E	F	G	H	I	J
Rx [200*(Rad(D1)] [mm]	RY [200*(Rad(E1)] [mm]	Rz [200*(Rad(F1)] [mm]	α [°]	β [°]	γ [°]	R [mm]	Cam's Angular θ [°]	Pressure Angle [°]	Displacement [y] [2.π.200.(H1)/360000] [m]
0.000	200.000	200.000	90	0	0	282.843	0	0.000	0.000
3.490	199.970	199.970	89	1	1	282.821	1	0.200	0.003
6.980	199.878	199.878	88	1	1	282.757	2	0.400	0.007

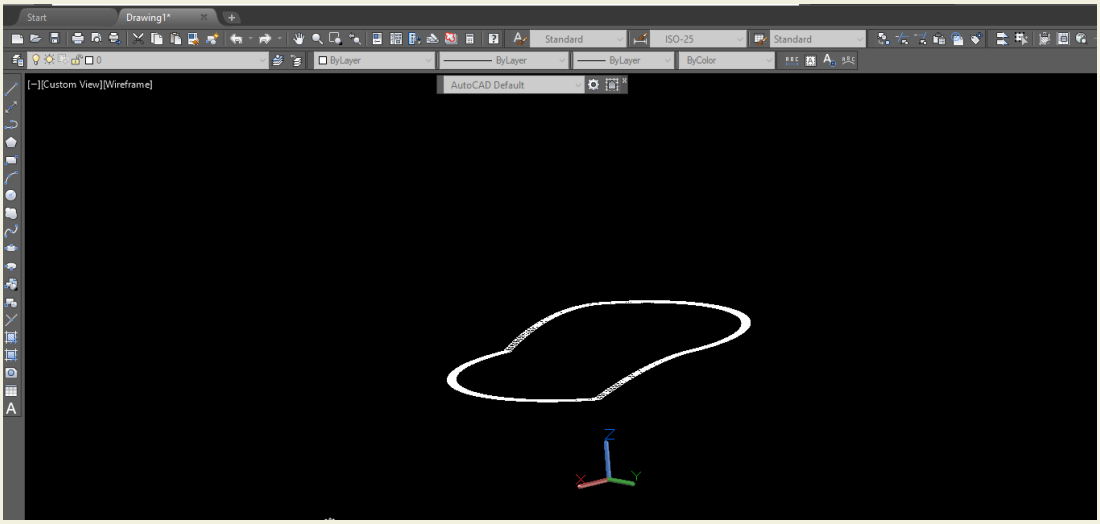

Figure 1. The groove profile generated on Autocad with Excel-VBA interaction

sed cylinder block was generated. The 3-D view of the designed cylinder is shown in Figure 3. In the design created in the VBA module within Autocad, ''AddCylinder'' command was used. Firstly, the initial point of the coded design is chosen on Autocad and then cylinder form is generated according to the radius value entered. The designs of many other forms in the Autocad library like cube, elliptical cylinder, sphere etc. can be generated with VBA-based studies. The codes of the system made for designing the camshaft and the cylinder in the VBA module are shown in Table 3 and Table 4.

Today, Visual Basic operations made through Microsoft Excel can be used not only in engineering, but also in many other fields like banking, companies carrying out statistical calculations, mathematics etc. From the engineering point of view, the most advantageous feature of this system is the ability of creating the drawing automatically in Autocad, where the calculations and coordinates of the system are generated by using a spreadsheet and a drawing software. Nowadays, in many engineering applications of 2-D and 3-D systems, Excel and design programs integrated with Visual Basic language are preferred [13].

2.2. Designing by Transferring the Excel Data to Autocad Command Line

Another way of generating drawings in Autocad by transferring the free data values from Excel is transferring the displacement coordinates of the follower onto Autocad. The X-Y-Z coordinate values given in Table 1 can be gathered in a single column with ="PO "&X1&","&Y1&","&Z1 command in a different column in Excel. The coordinate values there are copied and pasted to the command line in Autocad. ''PO'' is chosen on account of Autocad's 'point' command. The same method can be used with other computer-aidedd drawing programs and for different mechanisms. For a correct design, knowing the positions in x-y-z coordinate system will be enough. The computer-aided drawing software Autocad enables this type of 3-D drawings with Excel.

The X-Y-Z coordinate values of the system with 200 mm radiused cylindirical cam mechanism, given in Table 1, which represent the movement plane of the follower in the groove, were transferred into Autocad by the method explained above and the form in Figure 4 was obtained.

After transferring to Autocad, as the points are very small, they might be difficult to observe. with ''Zoom'' and ''Extents'' commands to be written in the command line, a closer inspection of the points will be possible. Besides, by writing ''DDPTYPE'' into command line, the format of the points can be changed. Finally, connecting all points will yield the 3-D design as shown in the figure below.

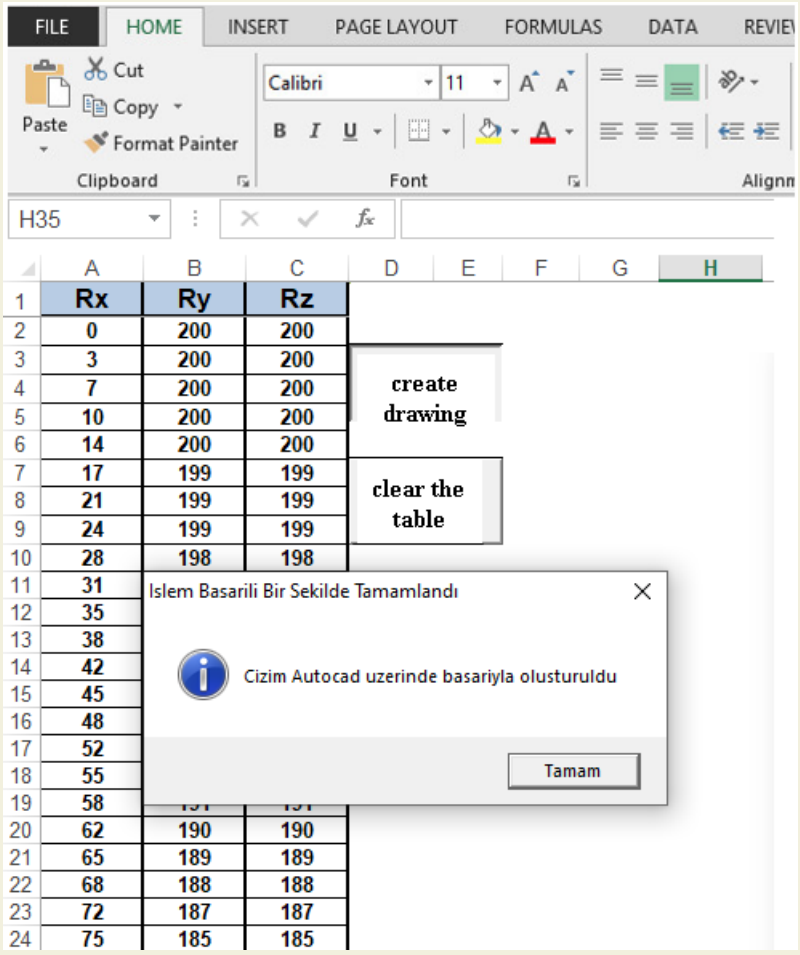

	A	B	C
1	Rx	Ry	Rz
2	0	200	200
3	3	200	200
4	7	200	200
5	10	200	200
6	14	200	200
7	17	199	199
8	21	199	199
9	24	199	199
10	28	198	198
11	31		
12	35		
13	38		
14	42		
15	45		
16	48		
17	52		
18	55		
19	58		
20	62	190	190
21	65	189	189
22	68	188	188
23	72	187	187
24	75	185	185

Figure 2. Excel table reflection of the 3-D groove profile

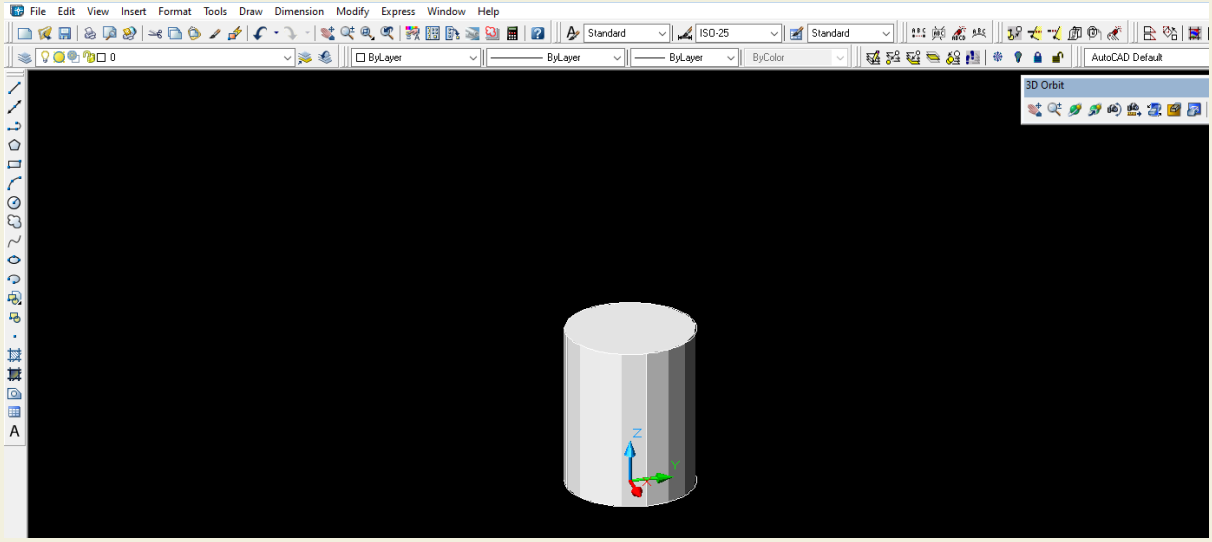

Figure 3. The cylinder design generated through Autocad VBA module

3. FINDINGS

In the design works by using Excel, Autocad, Solidworks and VBA programs[6], the cylindirical cam mechanisms used in poultry processing units were taken to be the model as the cylindirical cam mechanisms are frequently utilized in these machines which are used for poultry slaughtering, defeathering and eviscerating processes. On these process lines, the work stations are connected with conveyor systems and with the help of cylindirical cams, the flow direction of the stations can be altered when required. Furthermore, thanks to the suitable structure of the cylindirical cam mechanism for working together with other mechanisms, the aforementioned operations

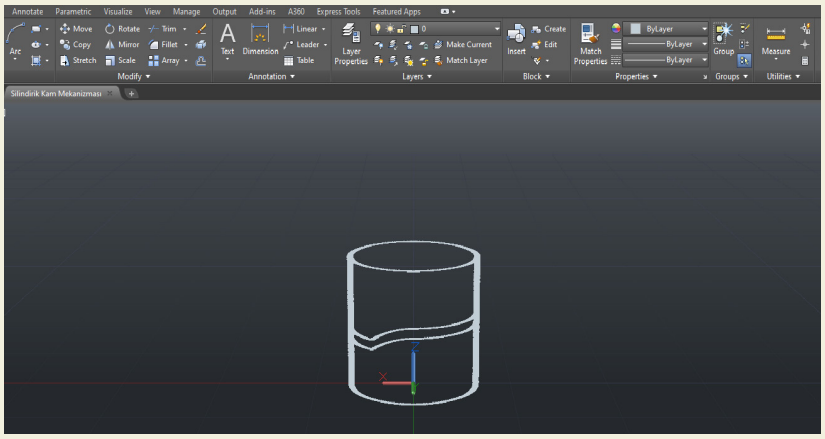

Figure 4. The cylindirical cam design generated by Excel and Autocad.

can easily be carried out with additional apparatus attached on the mechanism. The radiuses of the cylindirical cams used in these machines, the production capacities of which varies from 2000 pcs/hour to 13500 pcs/hour, changes between 90 cm and 600 cm. Depending on the operation conditions, number of followers on the mechanism can vary between 8 and 28 pcs. The followers in the system are enabled to be supported with hydraulic apparatus and they should be placed with 15-25 cm intervals being in conformity with the synchronous operation of the followers. In poultry processing machines, the followers operate with a speed between 2 rpm and 10 rpm depending on it's function.

As an example for designers and users, in order the data to be analyzed and to be compared correctly, analytical calculations were made for two different cylindirical cam mechanisms with 200 mm and 300 mm radiuses, in accordance with the given intervals, and the scaled designs were generated for these two radius values by using computer-aided programs. After the analytical calculations have been completed, the 3-D design of the cylindirical cam with 200 mm radius was made by co-using Excel-Autocad and Visual Basic language together; while 3-D design on Solidworks computer-aided program was utilized for the system with 300 mm radiused cylindirical cam.

During the design and calculations, the contact of the cam and the follower should be permanent for a proper motion. This continuous contact is analyzed through the pressure angle. In order the cam mechanisms to operate properly and safely, the pressure angle is chosen to be 30 degrees or less. Cam's radius, the speeds of the cam and the follower, and cam angle are the most important factors afeecting the pressure angle. The effect of these variables on the pressure angle is analyzed in detail in Table 2.

From the two systems with two different radiuses, of which the analytical calculations have been completed and the working parameters were analyzed, 7.93 degree for 200 mm radius and 11.8 degree for 300 mm radius were obtained to be the presure angle values. As these figures are below 30 degrees the angle value for steady operation of the cam mechanism, they are sutiable for steady running of the system. Besides, these results also prove that the pressure angles of the cylindirical cam mechanisms are quite less than 30 degrees.

Within this study, after scrutinizing the design details of the cam mechanisms, the advantages and superiorities of the cam mechanisms are also discussed. On the contrary of many other cam mechanisms, different analytical and graphical designs, derived from the classical motion diagrams by David Myszka, have been used for cylindical cam mechanisms, which moves in three dimensions.

In recent years, technological developments impacted also in the design and production of the cam mechanisms. Today, computer-aided drawing softwares like Autocad, Catia, Solidworks are used efficiently in designing cam mechanisms. Transferring the free data onto Excel tables and using the programming languages like VBA ease designing for users. In the analytical design step, the users can also use "BorlandDelphi7" (as in the post-graduate thesis "Computer Aided Cam Design and Produtciton of a Sample Cam Mechanism" of Murat Koyunbakan) or "Fortran IV" (as in the post-graduate thesis "Cam Mechanisms and Designing Them by Computer" of Günay Emirdağ) programming languages. These computer-aided designs provide the users with more reliable, safer and more accurate results by an easier method.

4. RESULT

The objective of this study is to provide an informative manual for the researchers about cam mechanisms and cylindirical cam mechanisms; and to present the superiorities of the cylindirical cam mechanisms over other cam mechanisms. The previous studies in the literature have been surveyed, and further on, computer-aided programs, which yield more detailed, more reliable and more accurate results, were preferred. With two design demonstrations generated by using them, it was shown that the designs made with Excel, Autocad, Solidworks and VBA programs have advantages with better possibilities.

Table 3. The code written in the VBA module for forming the cam way

```
Subcreate drawing()
        'Declaringthenecessaryvariables.
   Dim acadApp       As Object
   Dim acadDoc       As Object
   Dim acadCircle    As Object
   Dim LastRow       AsLong
   Dim i             As Long
   Dim Point(0 To 2)   As Double
        'Activatethecoordinatessheetandfindthelastrow.
WithSheets("Coordinates")
      .Activate
LastRow = .Cells(.Rows.Count, "A").End(xlUp).Row
EndWith
        'Checkiftherearecoordinatesfor at leastonepoint.
IfLastRow< 2 Then
MsgBox "Therearenocoordinatestodraw a point!", vbCritical, "Point Coordi-
natesError"
ExitSub
EndIf
      'CheckifAutoCADapplication is open.
   On ErrorResumeNext
   Set acadApp = GetObject(, "AutoCAD.Application")
      'IfAutoCAD is not openedcreate a newinstanceandmake it visible.
IfacadApp Is NothingThen
      Set acadApp = CreateObject("AutoCAD.Application")
acadApp.Visible = True
EndIf
      'Check (again) ifthere is an AutoCADobject.
IfacadApp Is NothingThen
MsgBox "Sorry, it wasimpossibletostartAutoCAD!", vbCritical, "AutoCADEr-
ror"
ExitSub
EndIf
   On ErrorGoTo 0
      'Ifthere is noactivedrawingcreate a newone.
   On ErrorResumeNext
   Set acadDoc = acadApp.ActiveDocument
IfacadDoc Is NothingThen
      Set acadDoc = acadApp.Documents.Add
EndIf
   On ErrorGoTo 0
   'Checkiftheactivespace is paperspaceandchange it to model space.
IfacadDoc.ActiveSpace = 0 Then '0 = acPaperSpace in earlybinding
acadDoc.ActiveSpace = 1 '1 = acModelSpace in earlybinding
EndIf
        'Loopthroughallthecoordinatesanddrawthecorrespondin-
gpoint(s).
WithSheets("Coordinates")
        'Set thepointtype.
acadDoc.SetVariable "PDMODE", .Range("E1").Value
          'Set thepoint size.
acadDoc.SetVariable "PDSIZE", .Range("G1").Value
                'Loopthroughallthecoordinates.
For i = 2 ToLastRow
              'Set thepointcoordinates.
        Point(0) = .Range("A" & i).Value
        Point(1) = .Range("B" & i).Value
        Point(2) = .Range("C" & i).Value
        'Draw thepoint.
acadDoc.ModelSpace.addpoint (Point)
Next i
EndWith
      'Zoom in tothedrawingarea.
acadApp.ZoomExtents
      'Releasetheobjects.
   Set acadCircle = Nothing
   Set acadDoc = Nothing
   Set acadApp = Nothing
      'Informtheuseraboutheprocess.
MsgBox "CizimAutocaduzerindebasariylaolusturuldu", vbInformati-
on, "IslemBasarili Bir SekildeTamamlandi"
EndSub
SubTabloyuTemizle()
      Dim LastRow As Long
      'Findthelastrowandclearalltheinput data..
WithSheets("Coordinates")
      .Activate
LastRow = .Cells(.Rows.Count, "A").End(xlUp).Row
      .Range("A2:C" &LastRow).ClearContents
      .Range("E1").ClearContents
      .Range("G1").ClearContents
      .Range("A2").Select
EndWith
EndSub
```

Table 4. The code written in the VBA module for forming the cylinder

```
Public Sub TestAddCylinder()
Dim varPickAs Variant
Dim dblRadiusAs Double
Dim dblHeightAs Double
Dim dblCenter(2) As Double
Dim objEntAs Acad3DSolid
'' set the default viewpoint
SetViewpoint
'' get input from user
With ThisDrawing.Utility
.InitializeUserInput 1
varPick= .GetPoint(, vbCr& "Pick the base center point: ")
.InitializeUserInput 1 + 2 + 4, ""
dblRadius= .GetDistance(varPick, vbCr& "Enter the radius: ")
.InitializeUserInput 1 + 2 + 4, ""
dblHeight= .GetDistance(varPick, vbCr& "Enter the Z height: ")
End With
'' calculate center point from input
dblCenter(0) = varPick(0)
dblCenter(1) = varPick(1)
dblCenter(2) = varPick(2) + (dblHeight / 2)
'' draw the entity
Set objEnt = ThisDrawing.ModelSpace.AddCylinder(dblCenter,
dblRadius, dblHeight)
objEnt.Update
ThisDrawing.SendCommand "_shade" &vbCr
End Sub
```

The most crucial issue in order the cam mechanisms to operate properly and smoothly is keeping the vibration, shake and pressure angle parameters under control. The pressure angle criteria should not exceed some specific limits for a stable operation. The figure of 30 degrees in the literature represents the limit value for an efficient operation. Cam mechanisms may be able to go on running beyond these points, however this will cause losses in the system rather than gains.

In the two systems, designs of which were made with Excel, Autocad, Solidworks and VBA programs, the pressure angle values for the cylindirical cam mechanisms with 200 and 300 mm radiuses have been obtained to be 7.93 degrees and 11.8 degrees respectively. As the follower moves within the groove in the cylindirical cam

mechanisms, the vibrations and shocks in the system are in minimum. Hence, the pressure angle value of cylindirical cam mechanisms are quite below 30 degrees when compared with other cam mechanisms. The obtained values also verify this fact.

In cylindirical cam mechanisms, under the same operation speed, the pressure angle value changes in parallel to the radius of the cam. The respective figures of 7.93 and 11.8 degrees for the systems with 200 mm and 300 mm radiused cylindirical cams attest this conclusion. In the cam mechanisms of poultry processing units, cam radius standards of which varies from 90 cm to 600 cm, as the radius increases, the negative effects of the cam angle on the pressure angle is observed more apparently. For the radiuses above the standard values or for the high cam angle values of the 600 mm radiused systems, the pressure angle goes beyond the safe values.

Some of the numerical values, obtained from the turning of the cylindirical cam, designed with computer-aided programs, one degree at a time, are given in Table 1 and Table 2. Poultry processing lines were taken as model for the two cylindirical cam mechanisms, design details of which are given. In the systems analyzed within the frame of these data, it was observed that the pressure angle is mostly affected by the cam's angular velocity and the cam angle. Among the systems studied, the ones with radiuses above the standard and with too high cam's angular velocities were found to have the maximum pressure angle values.

All numerical results, which are nor seen in Table1 and Table2, provide us with a foresight for the steady operation intervals for cylindirical cam mechanisms. In the light of these tables, the most important variables affecting the operation of cam mechanisms are cam radius, cam angle, and the speeds of the follower and the cam. The effects of these variables to the operation of the mechanism are analyzed in Table1 and Table2 with different values. As seen in the tables, in order to avoid the increase in the pressure angle which is caused by the increase in the cam radius, the linear speed of the follower can be increased or the cam angle can be reduced. The pressure angles of the systems, where the radius is chosen as small as possible and the choice of speeds are made properly, considering the synchronous motion of the follower and the cam mechanism, give the user an advantage by means of safe operation of the cylindirical cams.

The most important problem encountered in the cylindirical cam mechanisms is the slips which occur during ascending and descending of the follower in the groove. To avoid this complications, the cams with conical cylinders can be used or the groove profile can be reduced. These topics are recommended for the further studies on cam mechanisms and cylindirical cam mechanisms.

It is important to choose the pressure angle value to be 30 degrees or less for the stability and safety of the system. Harold Rothbard mentioned in his "Cam Design Handbook" that under light loads and in the working environment with low friction, this safe operation pressure angle value may go up to 47.5 degrees. For the future experimental studies on cam mechanisms, verification of these figures is recommended.

In our country, the production of both cylindirical cam mechanisms and cam mechanisms is not sufficiently developed. High setup costs of CNC and special cam machines, used in the production of cam mechanisms, can be mentioned as the main cause of this situation. Considering the production accuracy and convenience of these machines, this high cost load on the manufacturers might be reduced by governmental incentives in the future. As mentioned also in this study, when compared with many other mechanisms; with their easy designing, simple functioning and wide field of usage, the financial support for the cylindirical cam mechanisms can be foreseen to be considerably feasible.

REFERENCES

[1] Sclater, N. (2011). Mechanisms and mechanical devices sourcebook. McGraw-Hill Education.

[2] Norton, R. L. (2002). Cam design and manufacturing handbook. Industrial Press Inc.

[3] Chen YF. (1982). Mechanics and design of cam mechanisms. Pergamon Press, USA.

[4] Orta Doğu Teknik Üniversitesi (2001). Açık ders uygulamaları. http://ocw.metu.edu.tr/mod/resource/view.php?id=1124.pdf.

[5] Jana, R. K., & Bhattacharjee, P. (2017). A multi-objective genetic algorithm for design optimisation of simple and double harmonic motion cams. International Journal of Design Engineering, 7(2), 77-91.

[6] Karaaslan B.H. (2020). Tasarımdan imalata düşey çoklu çıkış uzuvlu silindirik kam mekanizması. Me.Ü. Fen Bilimleri Enstitüsü Y.Lisans Tezi. Türkiye.

[7] Harold A. R. (2004). Cam Design Handbook. Dean Emeritus College of Science and Engineering Fairleigh Dickinson University Teaneck, New Jersey, s. 1-58.

[8] Chakraborty, J., Dhande, S. G. (1977). Kinematics and geometry of planar and spatial cam mechanisms, JohnWiley & Sons, New York.

[9] Dhande, S. G., Bhodoria, B. S., Chakraborty, J. (1975). A unified approach to the analytical design of three dimensional cam mechanisms. Journal of Engineering for Industry, 97:327–333.

[10] MA, G. (1994). Synthesis of Contact Surfaces of Spherical Cam-Oscillating Roller-Follower Mechanisms: A General Approach. Journal of Mechanical Design, 116(1), 315-31

[11] Yan, H. S., & Chen, H. H. (1994). Geometry design and machining of roller gear cams with cylindrical rollers. Mechanism and Machine Theory, 29(6), 803-812.

[12] Tasy, D. M. and Hwang, G. S. (1994). Application of the theory of envelope of the determination of camoid profiles with translating followers. ASME J. Mech. Des., 116, s.320–325.

[13] Sutphin J. (2005). Autocad 2006 VBA: A Programmer's Reference. New York, ABD, s.143-203.

EUROPEAN MECHANICAL SCIENCE
e-ISSN: 2587-1110

Research Article

An experimental investigation of formability of inconel sheet plate for different die angles and rolling directions in press brake bending

Koray Hayrat[1], Ergin Kosa[1*], Şenol Durmuşoğlu[2]

[1]Beykent University, Faculty of Engineering and Architecture, Mechanical Engineering Department, Istanbul, Turkey, 34398
[2]Piri Reis University, Maritime Higher Vocational School, Mechatronics (Electro Technical Officer) Programme, Istanbul, Turkey, 34940

ORCID: K.Hayrat (0000-0002-8353-5697), E. Kosa (0000-0002-4607-4115), Ş. Durmuşoğlu (0000-0003-3232-8484)

Abstract: The formability of Inconel materials is important due to being used in engineering applications of aircraft and maritime. The aim of study is to investigate the bending characteristics and formability of Inconel 625 material having a property of corrosion resistance and high strength. In the paper, spring-back behavior of Inconel 625 sheet plates was examined in different die angles and orientations experimentally. The die angle was altered from 90˚ to 150˚ to and the different rolling directions of 0˚ and 90˚ were chosen to investigate the effect of grain orientation on spring-back of Inconel sheets. The bending radius was set as 2 mm for all bending tests. As a result, the spring-back angles and amounts were measured. Results show that as the bending angle is increased, the spring-back angle is decreased averagely from 3.35˚ to 2.58˚ for 0˚ rolling direction and maximum spring-back angle is obtained at a die angle of 120˚ for rolling direction of 90˚. Finally, Erichsen cupping test was also applied to determine the deformability of Inconel sheets. It was found that cup height value is 17.20 mm.

Keywords: Spring-back, Inconel, formability, die angle, bending press.

1. INTRODUCTION

Forming is commonly used plastic deformation process in manufacturing [1]. Bending is one of the significant and common forming methods in industrial applications [2]. There are many methods to bend the materials and researches had been studied on spring-back behavior in processes of V-bending [3, 4], U-bending [5, 6], tube bending [7], deep drawing [8], rubber forming [9], multi-point forming [10], stretching [11]. To form sheet plates and tubes, there are many parameters affecting the formability such as rolling direction [12], die angle [13], die width [14], bending radius [15], material thickness [15], temperature [16, 17], punch contact time [18], speed of punch [19, 20], strength coefficient [21], strain hardening coefficient [22], young's modulus [23]. In bending process, the main encountered problem is spring-back behavior of formed material [24]. Spring-back problem is about the elastically recover of the material [25]. Inconel 625 is one of the materials used in many engineering fields due to high strength and high corrosion resistance in marine mediums. The novelty of this research is that the effect of die angle on spring-back behavior of Inconel 625 sheet plate has not been investigated before and the formability of Inconel 625 sheet has been studied in Erichsen cupping test in the study.

There are some researches in literature realized by experimentally [26] and/or numerically [27, 28] to investigate the spring-back behavior of the materials in different types of bending processes [29]. Kumar et al. determined spring-back amount of aluminum sheet metal by using process of L – bending according to the gap between punch and die. The specimen sizes were 60 mm x 20 mm. Also, applied load was adjusted with respect to the thickness of specimens changing from 1 to 3 mm. It was found that as the gap is increased, the spring-back angle is increased [30]. Davoodi and Zareh-Desari used multi-forming method to bend aluminum alloy, 304 stainless steel and pure copper were tested by using V-shape and Sin-shaped dies. Experimental and numerical results were compared, and it was observed that increase in sheet thickness lowers the spring-back angle [31]. Buang et al. chose air v-die bending to determine spring-back behavior of steel sheets and changed the die and punch radius from 5 mm to 12.5 mm to find the spring-back angle. The results demonstrated that spring-back angle increased from 5.20˚ to 8.8˚ for the 5 mm of constant

* Corresponding author.
Email: erginkosa@beykent.edu.tr

European Mechanical Science (2023), 7(1): 29-34
https://doi.org/10.26701/ems.1132428
Received: June 18, 2022 — Accepted: December 5, 2022

die radius and from 7.19˚ to 7.25˚ for the 5 mm of constant punch radius [32]. Saito et al. focused on influence of temperature, punch speed and holding time on spring-back angle of high strength steel. Increase in temperature lowered the spring-back angle for both punch speeds of 0.02 mm/s and 20 mm/s in U-die forming. Also, because of stress relaxation, the bending angle reduced from 100.91˚ to 97.62˚ in 5 seconds at the beginning in V-die forming drastically [33]. Qudeiri et al. investigated the influence of yield stress and young's modulus on spring-back behavior of metallic sheets. An Increase in Young's modulus from 180 GPa to 230 GPa lowered the spring-back amount. In contrast, spring-back angle decreased as the yield strength of material increased from 200MPa to 400MPa. It was claimed that higher strength coefficient provides to withstand plastic deformation and higher modulus of elasticity causes to resist elastic deformation [34]. Gupta et al. analyzed the die width effect on spring-back behavior of CR4 steel. Also, 1 mm thick CR4 steel was coated by electro galvanizing. Die width and coating thickness was changed from 40 mm to 80 mm and from 0 to 10 μm, respectively. It was obtained that spring-back is lowered as the die width and coating thickness reduce [14]. Choi et al. used rebar bending machine to form structural steel and changed size of rebar, radius of bending, yield strength and friction coefficient to determine the effect of the factors on spring-back. The bending process was modelled numerically. It was calculated that as the coefficient of friction increased from 0.15 to 0.35, the spring back angle decreased from 2.55˚ to 2.21˚ in finite element analysis and increase in initial yielding strength increased the spring-back angle for bending angles of 95˚, 135˚ and 175˚ [35].

2. MATERIALS AND METHOD

2.1. 2.1 Bending process at Press Brake Machine

In the study, Press Brake Machine was used to bend Inconel 625 sheet metals due to being a simple machine and having a capability of various deforming types for designs as shown in figure 1. In bending process, tensile stresses are formed at the outer side of the sheet metal, the inner side of the sheet is forced by compressive forces. It is assumed that there is no change in the thickness of sheet metal theoretically. There is a die, punch and sheet metal in V-bending as illustrated in figure 2. The sheet metal elastically deforms back to recover after V-bending. Minimum bending force to form the sheet material is evaluated by using equation 1 theoretically whereas P is the bending force, th is the thickness of sheet plate, σ_t is the tensile strength of sheet material, bl is the width of the plate, c is the bending force coefficient and dw is die clearance [36].

$$P = \frac{c\sigma_t th^2 bl}{dW} \quad (1)$$

2.2. Material and Experimental Set up

Inconel 625 sheet metal was used in press brake bending operations. Because press brake bending machine are intensively used in industrial applications. Inconel 625 contains high Nickel and Chromium elements as given in table 1. Thus, Inconel 625 shows a resist to corrosion. So, it is used in transportation applications as a pipe material. In press brake bending, for each of the test samples, the die punch tries to reach the maximum force limit defined previously in the press brake by moving in the same direction and descending from top to bottom at a constant speed. The punch contacts the sheet material and starts to compress and bend the sheet metal according to the die shape. The automation program of the press reaches the maximum force and the defined bending angle simultaneously, and the bending process is completed, and the die angle was varied from 90˚ to 150˚ for both rolling directions of 0˚ and 90˚. All the operations were repeated four times by considering the same machine settings for each die angle and rolling direction,

Table 1. Chemical Composition of Inconel 625

Material	C	Mn	Fe	Sn	Si	Ni	Cr
% Value	0,02	0,15	3,21	0,00	0,19	61,22	22,37
Material	Al	Ti	Co	Mo	Nb	Ta	P
% Value	0,12	0,21	0,09	8,87	3,54	0,01	0,007

Table 2. Experimental Parameters

Definition	Case	Property
Bending Radius	Constant	2 mm
Die Angle	Variable	90 ° 120 ° 150 °
Material Type	Constant	Inconel 625
Material Thickness	Constant	1.00 mm
Rolling Direction	Variable	0 ° 90 °

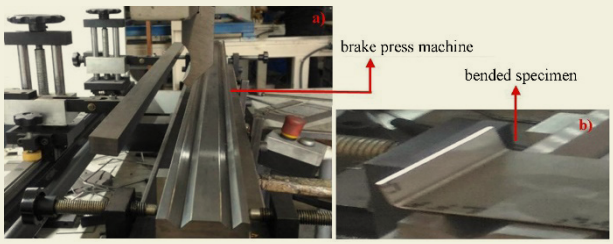

Figure 1. a) Bending Operations are performed in Press Brake, b) bent specimen.

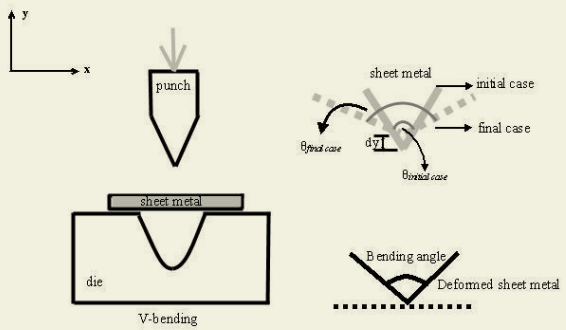

Figure 2. V-Bending and spring-back phenomena

respectively, and bending operations were carried out to determine the amount of spring-back. The thickness of sheet specimens is 1 mm for all tests. The size of the sheet plates is 50 mmx 80mm. Sheet plates were prepared by laser cutting. The experimental parameters are given in table 2.

3. RESULTS AND DISCUSSION.

3.1. Effect of Die Angle and Rolling Direction on Spring-back Angle

The behavior of spring is evaluated based on spring-back angle, Δθ, using the following equation 2;

$$\Delta\theta = \theta_{initial\ case} - \theta_{final\ case} \quad (2)$$

where $\theta_{initial\ case}$ is the angle during loading while $\theta_{final\ case}$ is the angle after unloading. 4 specimens were prepared to bend for each die-angle. Anisotropy is one of the reasons that sheet metal demonstrates different mechanical behavior along different directions. Thus, Bakhshi-Jooybari et al. chose CK 67 steel sheet and bent in different orientations to examine anisotropy factor [38]. To investigate anisotropy effect on spring-back behavior, sheet metal was bent in different rolling directions. The measured spring-back angles of 4 specimens for rolling directions of 0˚ and 90˚ are compared in figure in 3-5.

The average spring-back angles and spring-back amount for both rolling directions of 0˚ and 90˚ are given in table 3.

As a result of the study, generally increases in the bending angle decrease the spring-back angle and the amount of spring-back. Also, Karaağaç showed that the more the sheet plate is bent and deformed, the more stress is occurred leading to cause the increase in springback angle [39]. Apart from this, it is seen that the choice of rolling direction also has a significant effect on spring-back. It is the fact that the rolling direction perpendicular to the bending front reduces the amount of spring-back because elastic recovery is lower for 90 orientation.

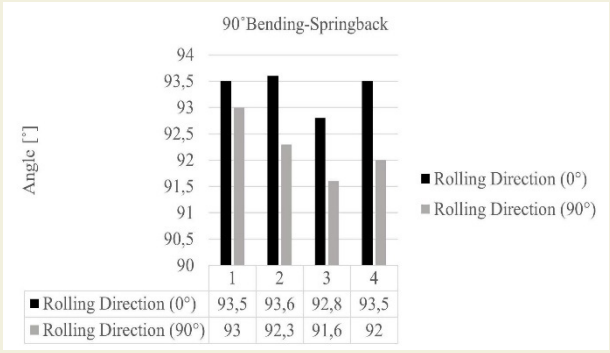

Figure 3. Angle after 90˚ bending for Rolling directions of 0˚ and 90˚

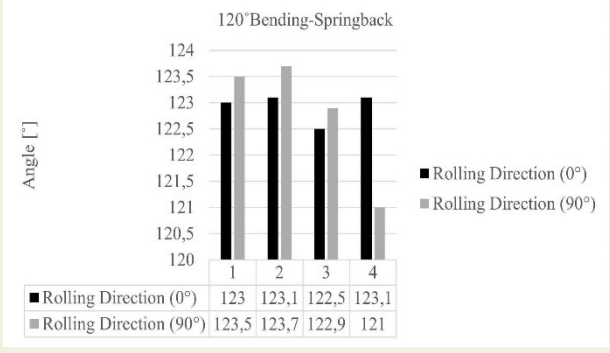

Figure 4. Angle after 120˚ bending for Rolling directions of 0˚ and 90˚

3.2. Erichsen Cupping Test and Tensile Test of Inconel 625 sheet metal.

To characterize mechanical properties of Inconel sheet plates in terms of forming ability, Erichsen Cupping test is applied. The test provides to specify the forming capacity of the material under multi-axial stresses. The test specimen is prepared according to standards of ISO 12004–2:2008. The size of sheet specimen as shown in figure 6-a is 10 mm x10 mm x1 mm. The sample prepared for the test was clamped and fixed in the jaw located in the middle of the machine. Afterwards, an increasing force was applied to the central part of the material by means of a die punch, and the material was started to be

Table 3. Spring-back angles at different conditions

Bending Angle	Sample No	Rolling Direction (0°)	Rolling Direction (0°)	Rolling Direction (90°)	Rolling Direction (90°)
		Ave.	Spring-back Amount (mm)	Ave.	Spring-back Amount (mm)
90°	1	3,35	2,796	2,23	1,879
90°	2				
90°	3				
90°	4				
120°	1	2,93	1,164	2,78	1,105
120°	2				
120°	3				
120°	4				
150°	1	2,58	0,927	2	0,719
150°	2				
150°	3				
150°	4				

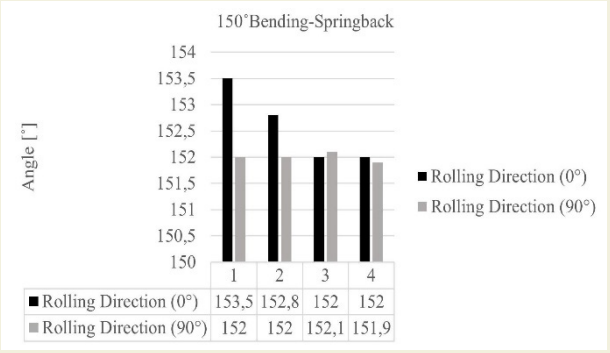

Figure 5. Angle after 150˚ bending for Rolling directions of 0˚ and 90˚

deformed.

The spherical punch moved to Inconel sheet plate to create permanent deformation until a crack formation occurred. 43.9 kN is applied to deform the sheet material and the fracture that is parallel to rolling direction is formed as shown in figure 6-b. Also, Matjaz et al. used low carbon steel to deep draw and observed that cracks were formed in longitudinal direction of rolling [40]. The depth value was found as 17.20 mm after Erichsen cupping test and it is compared with DP 780 in table 4 [37]. A higher depth of cut represents the higher formability. In addition to that, tensile specimen was used to characterize mechanical properties of Inconel sheet. Inconel 625 material tensile specimen was prepared in units of mm according to TSE ISO 6892 Standards as illustrated in figure 7. The test result shown in figure 8 is that ultimate tensile strength is 920 Nmm-², the yield strength is 474 Nmm-², and the elongation amount is 52.7%.

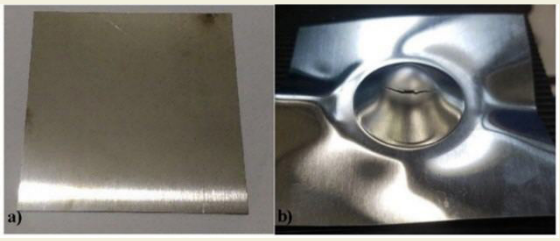

Figure 6. a) The specimen is prepared for Erichsen cupping test, b) Crack formation after the specimen is deformed in Erichsen cupping test.

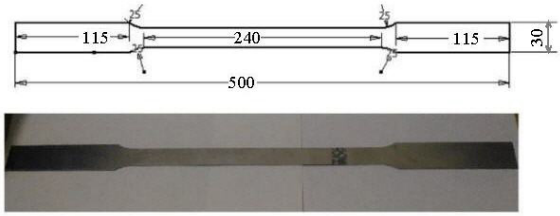

Figure 7. The dimensions of specimen used in tensile test

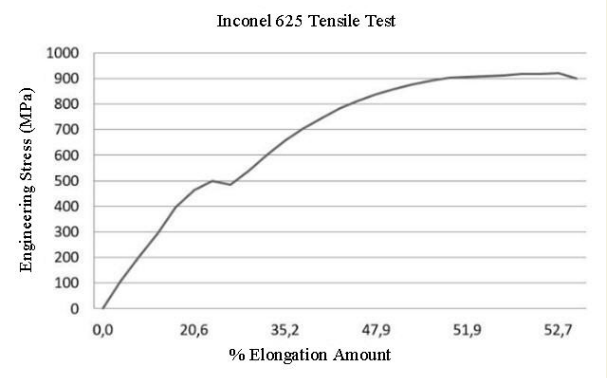

Figure 8. The yielding curve of Inconel 625 sheet plate.

Table 4. Comparison of Inconel 625 and DP 780 in Erichsen Cupping Test

Material Type	Thickness (mm)	Erichsen Cupping Test Value (mm)
Inconel 625	1.00	17.20
DP 780 [37]	1.00	8.24

4. NOMENCLATURE

P	Bending force, N
th	Thickness of sheet plate, mm
	Tensile strength, Nmm^{-2}
bl	width of plate, mm
c	Bending force coefficient
dw	Die clearance, mm
$\Delta\theta$	Spring-back angle
$\theta_{initial\ case}$	Initial angle
$\theta_{final\ case}$	Final angle

5. CONCLUSIONS

The study was focused on formability of Inconel 625 sheet metal for different die angles. It provides high strength and high corrosion resistant for both applications of aircraft and marine medium. Also, spring-back is a significant problem to form the sheet material. The bending amount can be adjusted according to spring-back character of material to form a desired geometry by predicting the spring-back amount. Thus, in the study the sheet metal spring-back behavior was characterized by using brake press bending machine for different bending angles and spring-back angles for each bending angle were measured by a goniometer. 4 specimens prepared for each bending angle was bent and the average of spring back angle of all 4 specimens were taken. Also, influence of rolling direction was investigated on spring-back behavior due to causing anisotropy. It is concluded that for rolling direction of 0° angle, the increase in bending angle from 90° to 150° lowers the average spring back-angle from 3.35° to 2.58°, experimentally. Tensile test results show that ultimate tensile strength is found as 920 Nmm-², the yield strength is found as 474 Nmm-² for Inconel 625 sheet metal for rolling direction of 0°. To characterize Inconel 625 sheet plate under multi axial stress, Erichsen Cupping Test was applied. 17.20 mm cup height was obtained until the fracture occurred and crack formed. It is also higher than AISI 304 stainless steel having an Erichsen index of 12 mm for 1.0 mm thickness [41]. So, Inconel 625 sheet metal has a capability of higher formability than the stainless steel [41].

6. REFERENCES

[1] Alghtani, A., Brooks, P. C., Barton, D. C., Toropov, V. V. (2018). Optimisation of Important Factors Influencing Spring-back after Sheet Metal Forming. International Journal of Applied Engineering Research, 13:16027-16035. DOI:10.37622/000000.

[2] Fan, L. F., Gou, J., Wang, G., and Gao, Y. (2020). Springback Characteristics of Cylindrical Bending of Tailor Rolled Blanks. Advances in Materials Science Engineering, https://doi.

org/10.1155/2020/9371808.

[3] Hai, V. G., Minh, N. T. H., and Nguyen, D. T. (2020). A study on experiment and simulation to predict the spring-back of SS400 steel sheet in large radius of V-bending process. Materials Research Express, 7(1), https://doi.org/10.1088/2053-1591/ab67f5.

[4] Leu, D-K., Hsieh, C-M. (2008). The influence of coining force on spring-back reduction in V-die bending process. Journal of Materials Processing Technology, 196: 230–235. https://doi.org/10.1016/j.jmatprotec.2007.05.033.

[5] Tong, V-C. and Nguyen, D-T. (2018). A study on spring-back in U-draw bending of DP350 high-strength steel sheets based on combined isotropic and kinematic hardening laws. Advances in Mechanical Engineering, 10(9):1–13. https://doi.org/10.1177/1687814018797436.

[6] Jung, J., Jun, S., Lee, H-S., Kim, B-M., Lee, M-G., and Kim, J. H. (2017). Anisotropic Hardening Behaviour and Springback of Advanced High-Strength Steels. Metals, 7:480.

[7] https://doi.org/10.3390/met7110480.

[8] Zhu, Y. X., Chen, W., Li, H. P., Liu, Y. L., Chen, L. (2018). Springback study of RDB of rectangular H96 tube. International Journal of Mechanical Sciences, 138–139:282–294. https://doi.org/10.1016/j.ijmecsci.2018.02.022.

[9] Lal, R. K., Choubey, V. K., Dwivedi, J. P., & Kumar, S. (2018). Study of factors affecting Springback in Sheet Metal Forming and Deep Drawing Process. Materials Today: Proceedings, 5: 4353–4358. https://doi.org/10.1016/j.matpr.2017.12.002.

[10] Chen, L., Chen, H., Guo, W., Chen, G., Wang, Q. (2014). Experimental and simulation studies of springback in rubber forming using aluminium sheet straight flanging process. Materials and Design, 54:354–360. http://dx.doi.org/10.1016/j.matdes.2013.08.050.

[11] Elghawail, A., Essa, K., Abosaf, M., Tolipov, A., Su, S., and Pham, D. (2017). Prediction of springback in multi-point forming. Cogent Engineering, 4(1): 1400507. https://doi.org/10.1080/23311916.2017.1400507.

[12] Slota, J., Gajdos, I., Spišák, E., Šiser, M. (2017). Springback Prediction of Stretching Process Using Finite Element Analysis for DP600 Steel Sheet. Acta Mechanica et Automatica, 11(1). https://doi.org/10.1515/ama-2017-0001.

[13] Hakimi, S., and Soualem, A. (2021). Evaluation of the sensitivity of springback to various process parameters of aluminum alloy sheet with different heat treatment conditions. Engineering Solid Mechanics, 9: 323-334. DOI: 10.5267/j.esm.2021.1.005.

[14] Ghimire, S., Emeerith, Y., Ghosh, R., Ghosh, S. (2017). Finite Element Analysis of an Aluminium Alloy Sheet in a V-Die Punch Mechanism Considering Spring-Back Effect. International Journal of Theoretical and Applied Mechanics, 12(2):331-342.

[15] Gupta, T. R., Sidhu, S. S., Payal, H. S. (2018). Effect of die width on spring back of electrogalvanized CR4 steel during air bending. Materials Today: Proceedings, 5:18416–18425. https://doi.org/10.1016/j.matpr.2018.06.182.

[16] Kartik, T., and Rajesh, R. (2017). Effect of Punch Radius and Sheet Thickness on Spring-back in V-die Bending. Advances in Natural and Applied Sciences, 11(8):178-183.

[17] Pornputsiri, N., Kanlayasiri, K. (2020). Effect of bending temperatures on the microstructure and springback of a TRIP steel sheet. Def. Technology, 16:980-987. https://doi.org/10.1016/j.dt.2019.11.018.

[18] Moon, Y. H., Kang, S. S., Cho, J. R., Kim, T. G. (2003). Effect of tool temperature on the reduction of the springback of aluminum sheets. Journal of Materials Processing and Technology, 132:365–368. https://doi.org/10.1016/S0924-0136(02)00925-1.

[19] Ma, Z., Tong, G. Q., Chen, F., Wang, Q., Wang, S. (2015). Grain size effect on springback behavior in bending of Ti 2.5Al-1.5Mn foils. Journal of Materials Processing and Technology, 224:11–17. http://dx.doi.org/10.1016/j.jmatprotec.2015.04.025.

[20] Choi, M. K., Huh, H. (2014). Effect of punch speed on amount of springback in U-bending process of auto-body steel sheets. Procedia Engineering, 81:963–968. https://doi.org/10.1016/j.proeng.2014.10.125.

[21] Krinninger M, Opritescu D, Golle R, Volk W. (2016). Experimental investigation of the influence of punch velocity on the springback behavior and the flat length in free bending. Procedia CIRP, 41:1066 – 1071. https://doi.org/10.1016/j.procir.2015.12.137.

[22] Sharad, G., Nandedkar, V. M. (2014) Springback in Sheet Metal U Bending-Fea and Neural Network Approach. Procedia Materials Science, 6:835–839. https://doi.org/10.1016/j.mspro.2014.07.100.

[23] Abdullah, S. A., Buang, M. S., Zulkpli, M. A., Mokhtar, F. R., Abdullah, H. (2018) Effect of Tensile and Material Properties on Springback Behavior of DP 590 Advanced High Strength Steel During Bending Process. International Journal of Engineering and Technology, 7:166-170. DOI: 10.14419/ijet.v7i4.18.21896.

[24] Zhang, R. Y., Zhao, G. Y., Guo, Z. H., & Quan, Y. P. (2015). Effects of material parameters on springback of 5052 aluminium alloy sections with hat profile in rotary draw bending. Internatonal Journal of Advanced Manufacturing Technology: 1067-1075. https://doi.org/10.1007/s00170-015-7056-8.

[25] Da Silva, E. A., Fernandes, L. F. V. M., Silva, J. W. D. J., Ribeiro, R. B., Pereira, M. D. S, Alexis, J. (2016). A Comparison between an Advanced High-Strength Steel and a High-Strength Steel Due to the Spring back Effect. IOSR journal of mechanical and civil engineering, 13(05):21-27. http://dx.doi.org/10.9790/1684-1305012127.

[26] Slota, J., Jurcišin, M., Dvorák, M. (2013). Experimental and Numerical Analysis of Springback Prediction in U-Bendings of Anisotropic Sheet Metals. Zeszyty Naukowe Politechniki Rzeszowskiej, Mechanika, 85[288], nr4:525-533.

[27] Srinivasan, R., and Raja, G. K. (2019). Experimental study on bending behavior of aluminium-copper clad sheets in V-bending process. Mechanics and Industry, 20:618. https://doi.org/10.1051/meca/2019059.

[28] Cho, J. R., Moon, S. J., Moon, Y. H., Kang, S. S. (2003). Finite element investigation on spring-back characteristics in sheet metal U-bending process. Journal of Materials Processing Technology, 141: 109–116. https://doi.org/10.1016/S0924-0136(03)00163-8.

[29] Panthi, S. K., Ramakrishnan, N., Ahmed, M., Singh, S. S., Goel, M. D. (2010). Finite Element Analysis of sheet metal bending process to predict the springback. Materials and Design, 31:657–662, https://doi.org/10.1016/j.matdes.2009.08.022.

[30] Jeong, H-S., Ha, M. Y., and Cho, J-R. (2012). Theoretical and FE Analysis for Inconel 625 Fine Tube Bending to Predict Springback. International Journal of Precise Engineering, 13(12): 2143-2148. https://doi.org/10.1007/s12541-012-0284-z.

[31] Kumar, K. D., Appukuttan, K. K., Neelakantha, V. L., Naik, P. S. (2014). Experimental determination of spring back and thinning effect of aluminum sheet metal during L-bending ope-

ration. Materials and Design, 56:613–619, http://dx.doi.org/10.1016/j.matdes.2013.11.047.

[32] Davoodi, B., Zareh-Desari, B. (2014). Assessment of forming parameters influencing spring-back in multi-point forming process: A comprehensive experimental and numerical study. Materials and Design, 59:103–114, http://dx.doi.org/10.1016/j.matdes.2014.02.043.

[33] Buang, M. S., Abdullah, S. A., and Saedon, J. (2015). Effect of Die and Punch Radius on Springback of Stainless Steel Sheet Metal in the Air V-Die Bending Process. Journal of Mechanical Engineering Science, 8:1322-1331, http://dx.doi.org/10.15282/jmes.8.2015.7.0129.

[34] Saito, N., Fukahori, M., Hisano, D., Hamasaki, H., Yoshida, F. (2017). Effects of temperature, forming speed and stress relaxation on springback in warm forming of high strength steel sheet. Procedia Engineering, 207: 2394–2398, https://doi.org/10.1016/j.proeng.2017.10.1014.

[35] Qudeiri, J. A., Khadra, F. A., Al- Ahmari, A., Umar, U. (2013). Effect of Material and Geometrical Parameters on the Springback of Metallic Sheets. Life Sciences, 10(2).

[36] Choi, C. H., Kulinsky, L., Jun, J. S., and Kim, J. H. (2014). A Numerical Study of the Spring-Back Phenomenon in Bending with a Rebar Bending Machine. Advances in Mechanical Engineering, 6: 959207. http://dx.doi.org/10.1155/2014/959207

[37] Suchy I. Handbook of Die Design. 2nd edn., McGraw-Hill, 2006, p.363.

[38] Santos, R. O., Pereira, A. B., Butuc, M. C., Vincze, G., Festas, A. J. and Moreira, L. P. (2020). Development of a Device Compatible with Universal Testing Machine to Perform Hole Expansion and Erichsen Cupping Tests, Machines, 8: 2. https://doi.org/10.3390/machines8010002.

[39] Bakhshi-Jooybari, M., Rahmani, B., Daeezadeh, V., & Gorji, A. (2009). The study of spring-back of CK67 steel sheet in V-die and U-die bending processes. Materials & Design, 30(7), 2410-2419. https://doi.org/10.1016/j.matdes.2008.10.018

[40] Karaağaç, İ. (2017). The experimental investigation of springback in V-bending using the flexforming process. Arabian Journal for Science and Engineering, 42(5), 1853-1864.

[41] Torkar, M., Tehovnik, F., & Podgornik, B. (2014). Failure analysis at deep drawing of low carbon steels. Engineering Failure Analysis, 40, 1-7.

[42] Inoxveneta (2022, October 31) Erichsen cupping test. https://www.inoxveneta.it/en/erichsen-index-cupping-test-values-tab/

EUROPEAN MECHANICAL SCIENCE
e-ISSN: 2587-1110

Research Article

Deposition and study of plasma sprayed Al_2O_3-TiO_2 coatings on AZ31 magnesium alloy

Tuğba Bayram[1], Muhammet Karabaş[2,3,*], Yusuf Kayalı[1]

[1] Afyon Kocatepe University, Metallurgical and Materials Engineering Dept., Afyonkarahisar, Turkiye.
[2] Kırklareli University, Faculty of Aeronautics and Space Sciences, Department of Airframe and Powerplant Maintenance, Kırklareli, Turkiye.
[3](former)Hakkari University, Materials Science and Engineering Dept., Hakkari, Turkiye.

ORCID: T. Bayram (0000-0003-1777-7863), M. Karabaş (0000-0002-0666-6132), Y. Kayalı (0000-0002-2449-7125)

Abstract: In this study, Al_2O_3, TiO_2 and Al_2O_3+ 3wt%TiO_2 coatings were deposited on AZ31 Mg alloy substrate by plasma spraying. The coatings were structurally characterized by scanning electron microscopy and X-ray diffraction. Corrosion experiments were carried out in 3.5% NaCl solution. Adhesion tests were performed according to Daimler Benz VDI-3198 standard. A coating layer of approximately 70 microns in thickness was deposited. High plasma enthalpy caused phase transformations in alumina-based ceramics. As a result of electrochemical corrosion study, it was determined that the coatings increased the corrosion resistance of AZ31 Mg alloy. While the most corrosion resistant coating is Al_2O_3+ 3wt%TiO_2, the weakest coating against corrosion is TiO_2. The adhesion behavior of all coatings to the substrate was at an acceptable quality level.

Keywords: Plasma spraying, Coating, Alumina, Titania, Corrosion

1. INTRODUCTION

Since magnesium (Mg) and its alloys are the lightest engineering materials, they are one of the candidate materials that are likely to be used in many applications. Mg and its alloys are noted for their low density, high specific strength, good machinability, high thermal conductivity, and good vibration and sound damping properties. With these features, it provides many advantages for use in automotive, aviation, home and office tools, chemical and energy industries. However, poor corrosion and wear resistance limits its use. To increase corrosion resistance of Mg, it is easiest to coat it. Many different coatings have been produced on Mg by different methods [1]. Besides cermet coatings such as WC–CrC–Ni and Cr_3C_2–NiCr, Al_2O_3, TiO_2 based coatings were applied with thermal spray to improve the surface properties of Mg and its alloys [2, 3]. Plasma spray stands out in the production of ceramic coatings with its features such as ease of processing and high coating quality. Plasma sprayed ceramic coatings have high adhesion-cohesion strength. In addition, plasma sprayed coatings do not need post-processes such as heat treatment. However, due to the high plasma temperature, it can be difficult to control the phase structure and purity of the sprayed material during the coating process. In addition, materials with low vapor pressure can evaporate in the plasma flame and non-stoichiometric coatings can be formed [4].

Alumina (Al_2O_3) ceramics are widely used in aggressive service conditions with their high temperature resistance, high fracture toughness, good abrasion resistance and good chemical stability. Al_2O_3 is one of the most industrially produced coatings by plasma spraying. Plasma sprayed Al_2O_3 coatings have been the subject of many studies. According to these studies, when Al_2O_3 is sprayed, it can undergo phase transformations due to high plasma enthalpy. Commercial Al_2O_3 powders are produced in the α- Al_2O_3 phase. However, δ and γ Al_2O_3 phases may occur due to phase transformation in coatings according to plasma spraying conditions. The general approach is that these phases do not strongly affect the coating characteristics. However, in some studies, it has been reported that these phases adversely affect the corrosion resistance of the coating in a long time. Titania (TiO_2) is another one of the most widely used ceramics as coating material with its dielectric, mechanical and chemical properties. When TiO_2 is sprayed with plasma, it decomposes depending on the process parameters. Sub-oxide phases may be formed in the coating structure. Therefore, phases with different O/Ti ratios occur. Researchers reported that this ratio is highly effective on the corrosion resistance of the coating [5]. TiO_2 is added between 3wt% and 40wt% to improve the corrosion resistance of Al_2O_3 ceramics against dilute acids. This process creates a phase with Al_2TiO_5 composition in the coating structure. Therefore, the coating structure includes Al-

* Corresponding author.
Email: mkarabas@itu.edu.tr

European Mechanical Science (2023), 7(1): 35-40
https://doi.org/10.26701/ems.1175394
Received: September 15, 2022 — Accepted: February 9, 2023

$_2TiO_5$ phase as well as Al_2O_3 and TiO_2 phases. This complex phase composition significantly affects the coating properties and provides extra corrosion resistance [6].

In this paper, the results of preliminary research are presented. The main aim of the study is to investigate coatability of AZ31 Mg alloy substrate with the Al_2O_3-TiO_2 by plasma spraying. Also, adhesion and corrosion behavior of the coatings was studied. Thus, lighter constructions can be produced by increasing the application field of Mg and its alloys.

2. MATERIALS AND METHODS

In this study, AZ31 Mg alloy sheets with 2mm thickness and 1 cm^2 surface area were used as substrate material. The chemical composition of the AZ31 substrate is given in table 1. The wt% level of alloying elements such as Al (2.5%-3.5%) and Zn (0.6%-1.4%) are in commercial norms [7]. Before the coating production process, the substrate materials were subjected to sandblasting. After that, the substrates were cleaned in an ultrasonic cleaner for 15 minutes in ethanol in order to remove surface contamination.

The cleaned substrates were fixed in the sample holder and get ready for the coating process. Commercial Metco 105 NS Al_2O_3, Metco 102 TiO_2 and Amdry 6200 Al_2O_3+3wt%TiO_2 powders were used as coating feedstock. SEM images and EDS analysis results of the feedstock powders are given in Figure 1. It is seen that the powders are in angular morphology. In addition, unexpected elements were not found in EDS analysis.

Sulzer Metco 9 MBM plasma gun was used in the deposition of the coatings. 730C was chosen as the gun nozzle. The gun speed and motion were adjusted by three-axis CNC robot. Plasma spraying process parameters are given in Table 2.

The microstructure, chemical composition of the feedstock powders and coatings were examined by field emission electron microscopy (SEM, JEOL JSM 7000F), which is equipped with an energy dispersive spectrometer. X-ray diffraction (XRD) with CuKα radiation (Bruker D8 Advance) was used to investigate the crystalline structure of the powders and coatings.

Electrochemical corrosion tests were performed in 3.5% NaCl solution. Measurements in electrochemical corrosion experiments were taken with Gamry reference 600 potentiostat/galvanostat ZRA. Calculations were made with Echem Analyst Soft software. Before starting the corrosion experiments, the samples were ultrasonically cleaned at 35°C with Acetone for 15 minutes, Ethanol for 15 minutes and double-distilled water for 15 minutes. Then it was dried in an oven at 50 °C for 1 hour. The cleaned samples were kept in 3.5% NaCl solution for 1 hour to stabilize. Afterwards, potentiodynamic corrosion experiments were started at room temperature in the same solution. Saturated Calomel Electrode (SCE) was used as the reference electrode. A 1 cm^2 Pt sheet was used as the counter electrode. Corrosion current (Icorr),

Table 2. Plasma spray process parameters.

Parametreler	
Current (A)	500
Primary gas flow rate,Ar (L/dk)	42.5
Secondary gas flow rate, H_2 (L/dk)	7
Carrier gas flow rate, Ar (L/dk)	6.4
Number of passes	12
Spray distance (mm)	75
Gun speed (mm/min)	200
Turntable speed (Hz)	50

Table 1. Chemical composition of AZ31 alloy (wt %).

Spectrum	Al	Zn	Mg	Other(Mn, Si Etc.)	Total
AZ 31	2.48	0.76	94.27	2.49	100.00

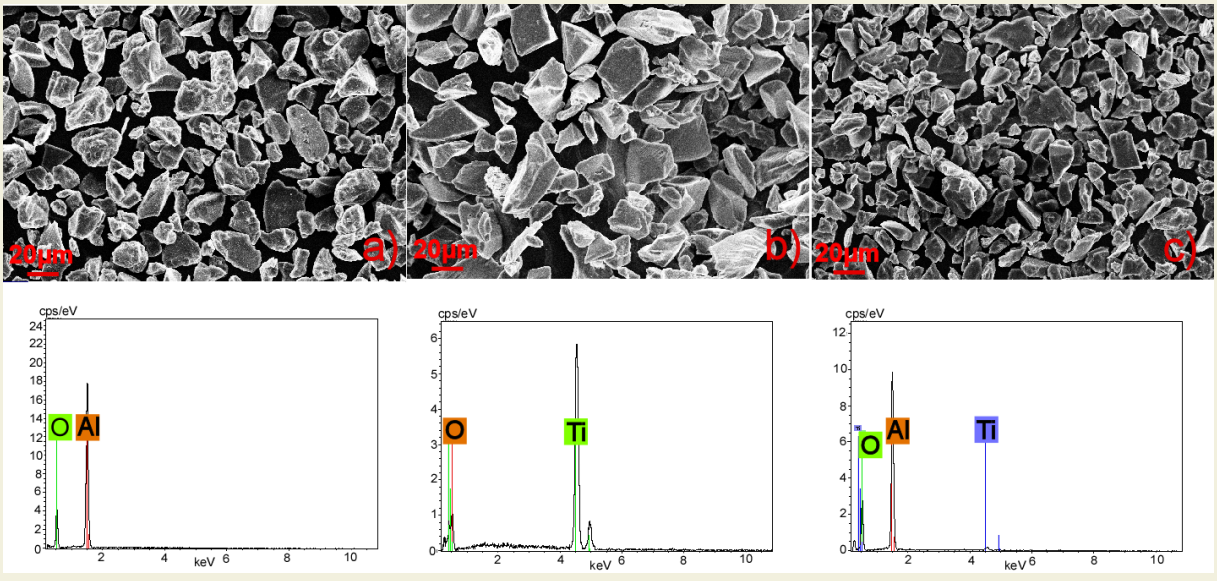

Figure 1. SEM images and EDS analysis graphs of the a) Al_2O_3, b) TiO_2, c) Al_2O_3+%3TiO_2 feedstocks.

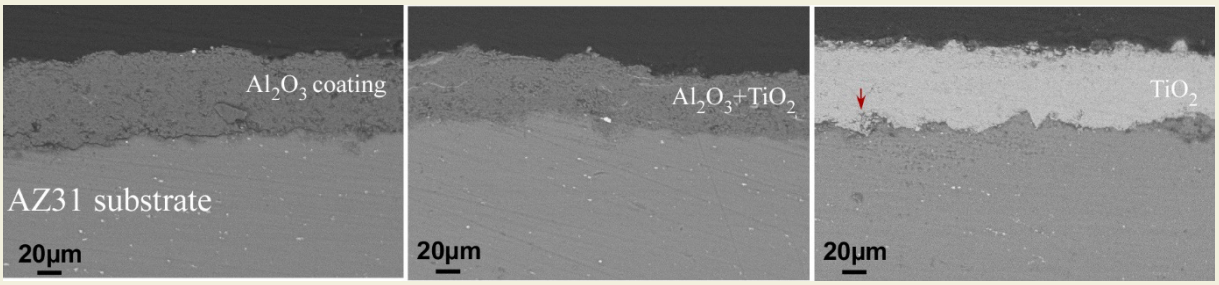

Figure 2. Cross-sectional SEM images of the coatings.

corrosion rate, Polarization resistance (Rp) and corrosion potential (Ecorr) values were recorded from current density-potential curves. Then, the corrosion current density (icorr) was found by dividing the corrosion current by the surface area.

The Daimler-Benz Rockwell-C adhesion test of the coatings was carried out by applying a 980 N load. The indentation zone was examined by SEM and the adhesion of the coatings according to the VDI 3198 standard was evaluated.

3. RESULTS AND DISCUSSION

3.1. Microstructure

The cross-sectional SEM images of the coatings deposited on the AZ31 substrate are given in Figure 2. Considering the adhesion behavior of the coatings to the substrate, it can be said that a crack-free and void-free coating-substrate interface is formed. In this case, a good adhesion regime for coatings can be mentioned. Coating microstructures have the traditional microstructural properties of coatings deposited by plasma spraying. The ceramic layers contain randomly distributed microporosities. A coating layer in the range of 60-70 μm thicknesses was accumulated.

3.2. Phase Structure

The XRD graphs of Al_2O_3 powder and its coating produced by plasma spraying are given in Figure 3. It was determined that the powder has an α-Al_2O_3 mostly phase structure. There is also a little δ-Al_2O_3 phase in powder form. As a result of spraying the powder, a serious phase transformation occurred due to high plasma enthalpy and rapid cooling. In addition, the peak heights decreased and the crystalline phases transformed to the amorphous phase structure. After spraying, δ-Al_2O_3 peak heights increased, α-Al_2O_3 peak heights decreased. The coating phase structure includes amorphous phase, δ-Al_2O_3 and α-Al_2O_3 phases [8, 9].

XRD diffraction patterns of TiO_2 powder and coating are shown in Figure 4. The phase structure of the powder includes two phases, rutile and anatase. When the coating phase structure is compared with initial feedstock powder, it is not possible to talk about a serious difference. No phase transformation occurred after plasma spraying. The coating also contains anatase and rutile phases as in powder [5, 10].

The XRD graphs of the Al_2O_3+3wt%TiO_2 powder and the coating are given in Figure 5. When the powder phase structure is evaluated, there is a phase structure with a majority of α-Al_2O_3. At low altitudes, δ-Al_2O_3 peaks are located. As a result of plasma spraying, a serious phase transformation occurred. It can be said that the α-Al_2O_3 phase turns into amorphous phase as a result of high plasma temperature and rapid cooling of the particles when they reach the substrate. While α-Al_2O_3 peak intensity decreased, δ-Al_2O_3 peak intensity increased because some α-δ Al_2O_3 conversion occurred. In addition, Al_2TiO_5 phase was formed as a result of Al_2O_3-TiO_2 reac-

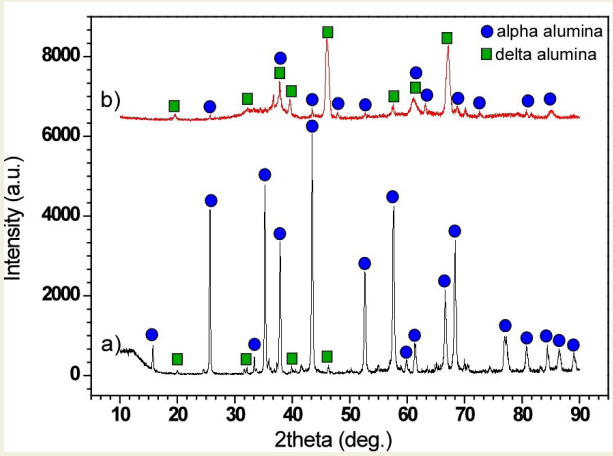

Figure 3. XRD graphs of the Al_2O_3 (a) powder and (b) coating.

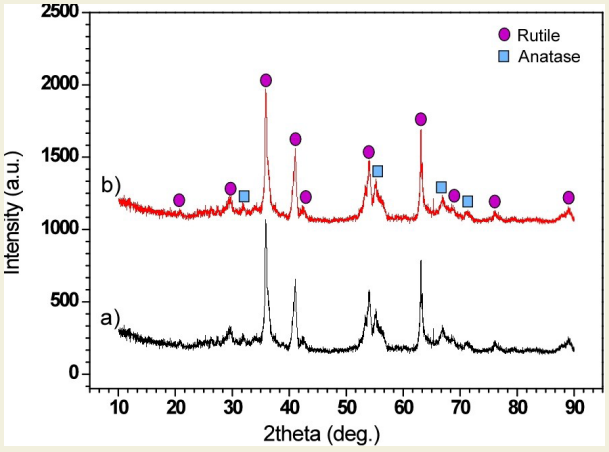

Figure 4. XRD graphs of the TiO_2 (a) powder and (b) coating.

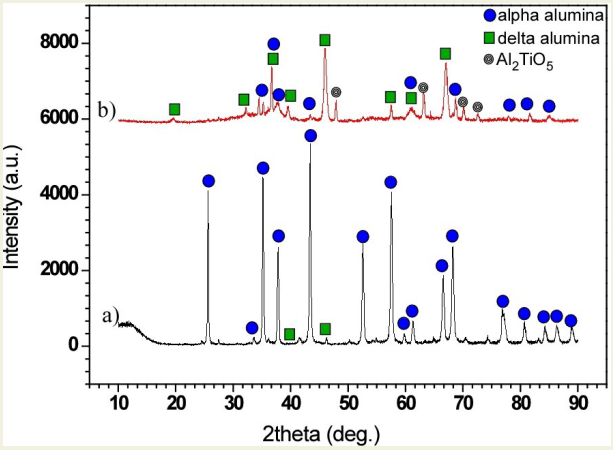

Figure 5. XRD graphs of the Al_2O_3+%3TiO_2 (a) powder and (b) coating.

tion during coating deposition by plasma spraying [8, 11].

3.3. Electrochemical Corrosion Tests

Corrosion variables calculated from the measurements taken during the corrosion tests are given in Table 3. The Icorr corrosion current appears to be highest in the substrate as expected. The corrosion current value decreased with the coating deposition. Among the coatings, the highest corrosion current value was calculated in TiO_2 coating, while the lowest corrosion current value was calculated in Al_2O_3+3wt%TiO_2 coating. On the other hand, the Rp value increased as a result of the coating of the substrate material depending on the Ecorr corrosion potential. While the lowest Rp value was in the substrate material, the highest Rp value was measured in the Al_2O_3+3wt%TiO_2 based coating. When the corrosion rates are evaluated, as expected, a serious decrease occurred as a result of the coating deposition. The corrosion rate of all coatings is lower than the uncoated AZ31 substrate. The highest corrosion rate was found in TiO_2 coating, and the lowest corrosion rate in Al_2O_3+3wt%TiO_2 coating. The Al_2TiO_5 phase in the Al_2O_3+3wt%TiO_2 coating phase structure caused a great decrease in the corrosion rate compared to the Al_2O_3 coating without TiO_2 additives [6]. The standard reduction potentials of aluminum and titanium are -1.66 V and -1.63 V, respectively. These values are very close to each other. This situation showed that the oxidation of Al and Ti in the coating increased in NaCl solution, and reacted with oxygen to form a coating + protective oxide layer on the AZ31 surface. These formations reduced corrosion. Although the Ecor value of the Al_2O_3+TiO_2 coating found from the Tafel curves (Figure 6) was close to AZ31, it was the best coating. The Al_2O_3 coating was more oxidized than TiO_2 and was the coating with the most positive Ecor value. However, the Al_2O_3+TiO_2 coating was slightly oxidized in solution.

Table 3. Corrosion variables of coated and uncoated AZ31 alloys.

%3.5 NaCl	AZ31	TiO_2	Al_2O_3	Al_2O_3+TiO_2
Icorr. (μA)	48.90	30.10	9.130	2.410
Ecorr. (mV)	-1510	-836	-303	-1310
Cor. Rate(mpy)	39.11	18.36	6.691	1.379
Rp(kΩ)	0.0766	12.42	15.97	17.71
Beta A (V/decade)	0.347	0.838	0.804	0.111
Beta C (V/decade)	0.162	2262	0.583	0.254

Figure 6 shows the tafel polarization curves drawn with the measurements taken during the corrosion tests. The gradient regime of the tafel zones and the variation of the polarization zones are consistent with the change in corrosion rates given in Table 3. While the slope of the anodic polarization curves of Al_2O_3 and TiO_2 coatings is higher, the slope of the cathodic polarization curves is higher in AZ31 substrate and Al_2O_3+3wt%TiO_2 coating. In other words, while reduction reactions are dominant in the corrosion of AZ31 substrate and Al_2O_3+3wt%TiO_2, oxidation reactions such as reduction and oxidation are also effective in Al_2O_3 and TiO_2 coatings.

Rp values are also compatible with icorr values. The fact that the Ecor values in all coatings go to more positive potentials shows that there is oxidation on the AZ31 surface with the coating. Anodic (β_a) and cathodic (β_c) Tafel slope values changed according to the properties of the coating material. The highest anodic and cathodic Tafel slopes were detected in the TiO_2 coated sample. However, TiO_2 coating was not as effective in preventing corrosion as Al_2O_3 and Al_2O_3+TiO_2 coating. It is a known fact that aluminum forms a passive film by forming oxide on the surface. The shapes of the Tafel curves are almost the same. This shows that the coatings do not change the corrosion mechanism, they only prevent corrosion by slowing down the anodic and cathodic reactions.

Surface EDX analysis results of the AZ31 and coatings are given in figure 7. It is seen that Na and Cl ions in the corrosion solution are absorbed to the surfaces. The rates of corrosion and the ratios of Na and Cl ions on the surfaces are directly proportional. Na and Cl ions have the lowest proportions and the highest amount of oxygen in the coated magnesium alloy with Al_2O_3+3wt%TiO_2 coating, which has the best corrosion resistance. In the sample coated with Al_2O_3+3wt%TiO_2, the ratios of Na and Cl

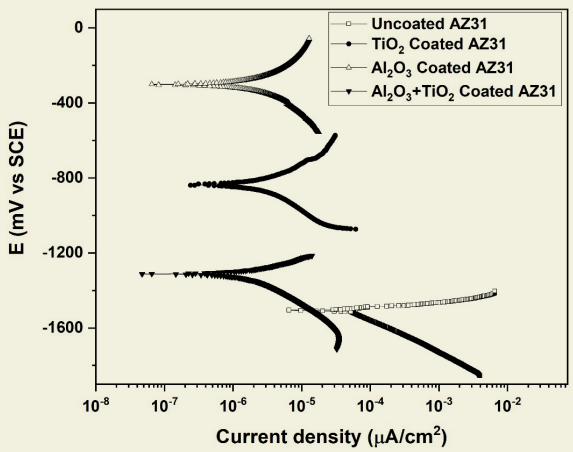

Figure 6. Tafel plots of coated and uncoated AZ31.

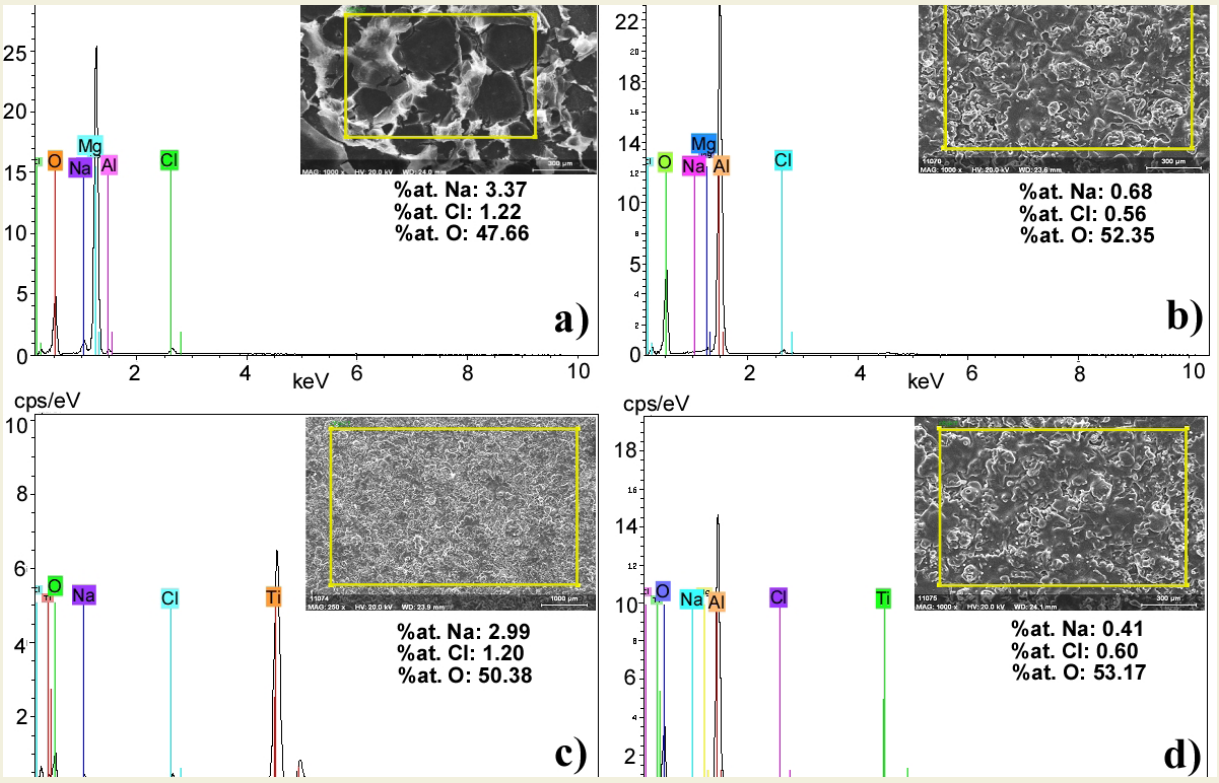

Figure 7. Surface EDX analysis results of the a) uncoated AZ31, b) Al_2O_3 coating, c) TiO_2 coating, d) Al_2O_3+3wt%TiO_2 coating.

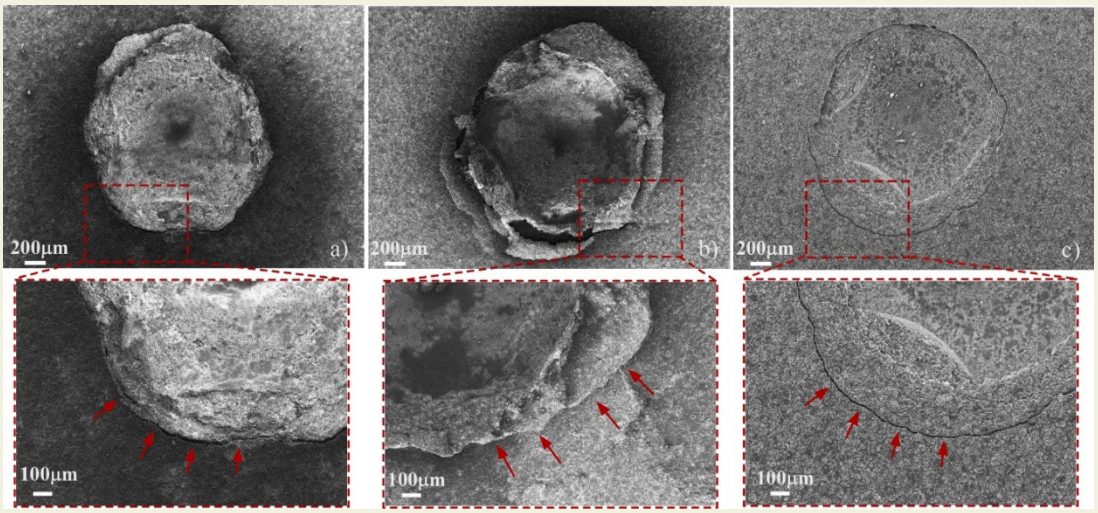

Figure 8. SEM images Rockwell C indentation zone a) Al_2O_3, b) TiO_2, c) Al_2O_3+%wt3TiO_2.

adsorbed to the surface are taken respectively. % Na: 0.41 and Cl: 0.60, the ratios are at least in the untreated magnesium alloy, which has the worst corrosion resistance. % Na:3.37 and Cl: 1.22. While the amount of oxygen on the surface in the uncoated magnesium alloy is 47.46, the amount of oxygen on the surface is 53.17 in the coated magnesium alloy with Al_2O_3+3wt%TiO_2 coating. This contributed to the passivation of the film on the surface by increasing the amount of oxygen on the surface. The film layer that provides this passivation must be sticky, non-porous, chemically inert. If there is a protective film on the coating, the substrate material will not be seriously damaged, corrosion or pitting will not occur, but if the film layer formed contains defects or is discontinuous, the substrate will corrode. To cause pitting, Cl-, SO_4-, Br-, I-, etc. Anions such as ions are adsorbed on the metal surface first. Then, they initiate active dissolution of the metal in the defects present on the metal surface. The presence of second phases where one of the phases has a different chemical composition, microstructure or the formation of micro cells, one of these phases will act as the cathode and the other as the active anode. This will cause preferential dissolution of the one phase acting as the active anode, resulting in preferential, localized dissolution in the material. Al-containing alloys are protected against corrosion by forming a protective layer of Al_2O_3, alumina [12].

3.4. Rockwell C Adhesion Tests

SEM images of the indentation regions are given in Figure 8. All of the coatings exhibited acceptable levels of damage. The damage to Al_2O_3 and TiO_2 is similar. In these coatings, an outward agglomeration occurred in the coatings with the indentation force. There is no separation and crack formation in the coating layer. This situation is directly related to the mechanical properties of the coatings such as fracture toughness and modulus of elasticity. In Al_2O_3+3wt%TiO_2, a circular crack was formed in the area where the indenter sank. Little plastic deformation occurred in the coating with the indentation force [13].

According to all these evaluations, it can be evaluated that all coatings have an acceptable level of adhesion strength. Damages are in HF3-HF4 class according to VDI-3198 standard.

4. CONCLUSION

In this study; AZ31 Mg alloy is coated with Al_2O_3-TiO_2 based ceramics by plasma spraying. Structural characterizations of these coatings were performed and their corrosion behavior was investigated. According to the experimental results, AZ31 Mg alloy can be used for a longer time with plasma sprayed Al_2O_3-TiO_2 coatings in corrosive environments. The lowest corrosion rate was calculated for Al_2O_3+3wt%TiO_2 coating, and the highest corrosion rate was calculated for TiO_2 coating. The adhesion strength of the all coatings is acceptable. However, adhesion strength tests with different methods and a more detailed examination of the coating-substrate interfaces are necessary for further studies. In addition, corrosion tests in more aggressive environments and the behavior of coatings under high temperature conditions can also be investigated. This paves the way for the use of Mg and its alloys in further constructive applications.

ACKNOWLEDGMENTS

This work was supported by Scientific Research Projects Coordination Unit of Hakkari University. Grant number: FM20BAP6.

6. REFERENCES

[1] Gray, J.E., Luan, B., (2002). Protective coatings on magnesium and its alloys — a critical review. Journal of Alloys and Compounds. DOI: 10.1016/S0925-8388(01)01899-0.

[2] Çelik, İ., (2016). Structure and surface properties of Al2O3–TiO2 ceramic coated AZ31 magnesium alloy. Ceramics International. DOI: 10.1016/j.ceramint.2016.05.162.

[3] Jonda, E., Latka, L., Pakiela, W., (2021). Comparison of Different Cermet Coatings Sprayed on Magnesium Alloy by HVOF. DOI: 10.3390/ma14071594.

[4] Heimann, R.B., (2008). Plasma-Spray Coating: Principles and Applications. Wiley.

[5] Gardon, M., Guilemany, J.M., (2014). Milestones in Functional Titanium Dioxide Thermal Spray Coatings: A Review. Journal of Thermal Spray Technology. DOI: https://doi.org/10.1007/s11666-014-0066-5.

[6] Toma, F.L., Stahr, C. L., Berger, M., Saaro, S., Herrmann, M., Deska, D., Michael, G., (2010). Corrosion resistance of APS- and HVOF-sprayed coatings in the Al2O3-TiO2 system. Fraunhofer IWS. DOI: 10.1007/s11666-009-9422-2.

[7] Shankar, S., Nithyaprakash, R., Abbas, G., Naveenkumar, R., Prakash, C., Pramanik, A., Basak, A., (2022). Tribological Behavior of AZ31 Alloy Against Si3N4 Using In-vitro and In-silico Submodeling Approach for Human Hip Prosthesis. DOI: 10.1007/s12633-022-02077-9.

[8] Michalak, M., Latka, L., Sokołowski, P., Candidato, R.T., Ambroziak, S., (2021). Effect of TiO_2 on the microstructure and phase composition of Al_2O_3 and Al_2O_3–TiO_2 APS sprayed coatings. DOI: 10.24425/bpasts.2021.136735.

[9] Mohammadian Bajgiran, M., Rezvani Rad, M., McDonald, A., Moreau, C., (2021). Microstructure, phase and dielectric strength of thermally sprayed alumina layers in coating-based heating systems. DOI: 10.1111/ijac.13731.

[10] Yusuf, Y., Ghazali, M.J., Juoi, J.M., Rahim, T.A., Mustafa, Z., (2022). Plasma-sprayed TiO2 coatings: Hydrophobicity enhanced by ZnO additions. DOI: 10.1111/ijac.14009.

[11] Basha G, M.T., Bolleddu, V., (2021). Characteristics of Thermally Sprayed Alumina-Titania Ceramic Coatings obtained from Conventional and Nanostructured Powders - A Review. Australian Journal of Mechanical Engineering, p. 1-22. DOI: https://doi.org/10.1080/14484846.2021.1876603.

[12] González-Rodriguez, J.G., Colín, J.C., Serna, S., Campillo, B., Albarran, J.L., 2007. Effect of macroalloying with Cu on the corrosion resistance of rapidly solidified NiAl intermetallic in 0.5 M H2SO4. Materials Science and Engineering: A. DOI: 10.1016/j.msea.2006.11.079.

[13] Vidakis, N., Antoniadis, A., Bilalis, N., (2003). The VDI 3198 indentation test evaluation of a reliable qualitative control for layered compounds. Journal of Materials Processing Technology. DOI: 10.1016/S0924-0136(03)00300-5.